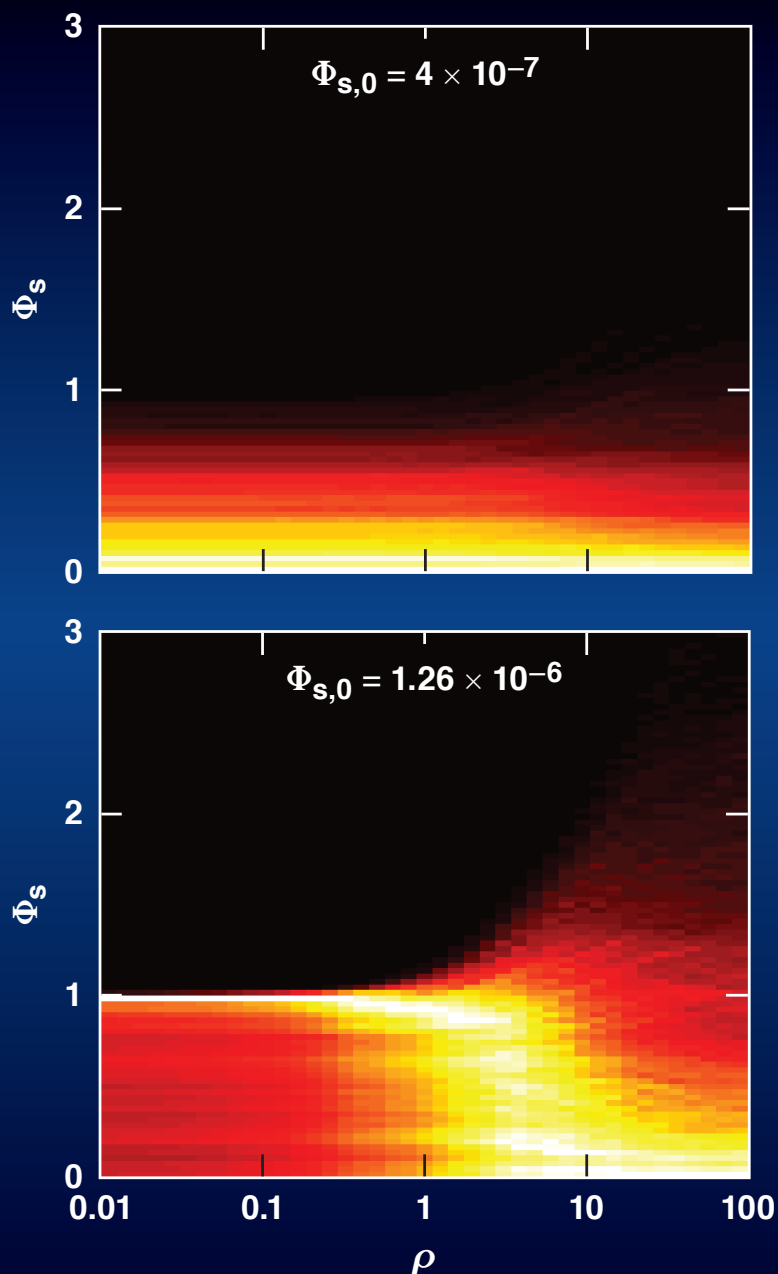


LLE Review

Quarterly Report

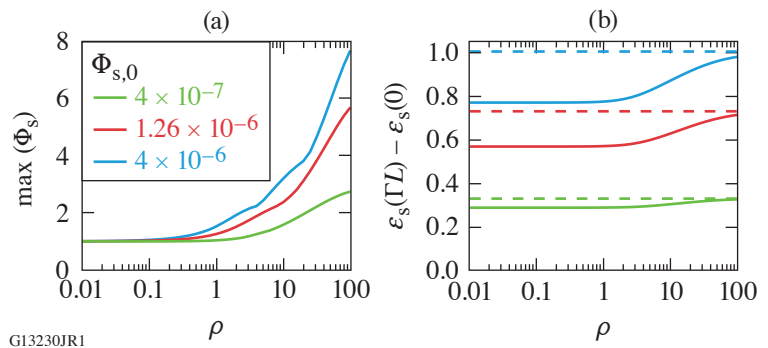


About the Cover:

Broadband spectrally incoherent pulses are promising to mitigate laser–plasma instabilities and beam imprint. Three-wave nonlinear mixing can amplify optical pulses over much larger bandwidth than laser amplification. The operation of optical parametric amplifiers (OPA's) with coherent pulses having smooth, slowly varying temporal profiles is well understood, but their operation with spectrally incoherent pulses having random high-frequency time-domain modulations has not previously been described in detail.

A framework based on normalized three-wave nonlinear mixing equations has been developed and used to analyze the operation of OPA's with spectrally incoherent pulses, showing that the temporal walk-off between signal, pump, and idler, as well as the relative photon flux of the pump and signal wave, play a critical role in the energy, bandwidth, and statistical properties of the amplified signal. The images on the cover show the evolution of the probability density function (pdf) of signal photon flux (Φ) as a function of the temporal walk-off between the signal and pump normalized to the signal's coherence time. In the absence of pump depletion (upper figure), the pdf remains a negative exponential function, as expected for an incoherent source. When the signal is sufficiently high to deplete the pump (lower figure), the pdf depends strongly on the pump-signal walk-off: the signal's photon flux is limited by the pump's photon flux at low temporal walk-off, but the signal can be amplified to much higher values if temporal walk-off allows it to deplete the pump over a range of times.

Parametric amplification leads to a clamping of the signal's temporal modulations for low pump-signal temporal walk-off, but the signal's intensity at certain times can be much larger than what can be obtained with coherent waves, particularly as the input signal intensity increases (a). The amplification efficiency for spectrally incoherent waves is lower than for coherent waves, but it converges to the same value for large pump-signal temporal walk-offs that allow for pump depletion in all time slots (b).



This report was prepared as an account of work conducted by the Laboratory for Laser Energetics and sponsored by New York State Energy Research and Development Authority, the University of Rochester, the U.S. Department of Energy, and other agencies. Neither the above-named sponsors nor any of their employees makes any warranty, expressed or implied, or assumes any legal liability or responsibility for the accuracy, completeness, or usefulness of any information, apparatus, product, or process disclosed, or represents that its use would not infringe privately owned rights. Reference herein to any specific commercial product, process, or service by trade name, mark, manufacturer, or otherwise, does not necessarily constitute or imply its endorsement, recommendation, or favoring

by the United States Government or any agency thereof or any other sponsor. Results reported in the LLE Review should not be taken as necessarily final results as they represent active research. The views and opinions of authors expressed herein do not necessarily state or reflect those of any of the above sponsoring entities.

The work described in this volume includes current research at the Laboratory for Laser Energetics, which is supported by New York State Energy Research and Development Authority, the University of Rochester, the U.S. Department of Energy Office of Inertial Confinement Fusion under Cooperative Agreement No. DE-NA0003856, and other agencies.

Printed in the United States of America

Available from

National Technical Information Services
U.S. Department of Commerce
5285 Port Royal Road
Springfield, VA 22161
www.ntis.gov

For questions or comments, contact Jessica Shaw, Editor, Laboratory for Laser Energetics, 250 East River Road, Rochester, NY 14623-1299, (585) 276-5618.

www.lle.rochester.edu

LLE Review



Quarterly Report

Contents

IN BRIEF	iii
INERTIAL CONFINEMENT FUSION	
Direct-Drive Laser Fusion: Status, Plans, and Future	169
Direct Measurements of DT Fuel Preheat from Hot Electrons in Direct-Drive Inertial Confinement Fusion	172
Validating Heat-Transport Models Using Directly Driven Spheres on OMEGA	174
Magnetic-Field Generation and Its Effect on Ablative Rayleigh–Taylor Instability in Diffusive Ablation Fronts	177
Self-Consistent Theory of the Darrieus–Landau and Rayleigh–Taylor Instabilities with Self-Generated Magnetic Fields	180
Transport Coefficients for Magnetic-Field Evolution in Inviscid Magnetohydrodynamics	183
PLASMA AND ULTRAFAST PHYSICS	
Kinetic Inflation of Convective Raman Scattering Driven by a Broadband, Frequency-Modulated Laser Pulse	186
Measurements of Non-Maxwellian Electron Distribution Functions and Their Effect on Laser Heating	189
Nonlinear Spatiotemporal Control of Laser Intensity	192
Laser-Plasma Acceleration Beyond Wave Breaking	195
HIGH-ENERGY-DENSITY PHYSICS	
Wide-Ranging Equations of State for B ₄ C Constrained by Theoretical Calculations and Shock Experiments	198

DIAGNOSTIC SCIENCE AND DETECTORS

A Novel Photomultiplier Tube Neutron Time-of-Flight Detector 201
A Generalized Forward Fit for Neutron Detectors with Energy-Dependent
Response Functions 205

LASER TECHNOLOGY AND DEVELOPMENT

Parametric Amplification of Spectrally Incoherent Signals 208
Comparison of the Laser-Induced–Damage Threshold in Single-Layer Optical Films
Measured at Different Facilities..... 211

USERS REPORT

The 12th Omega Laser Facility Users Group Workshop 214

LASER FACILITY REPORT

FY20 Q4 Laser Facility Report 216

PUBLICATIONS AND CONFERENCE PRESENTATIONS

In Brief

This volume of LLE Review 164 covers the period from July–September 2020. Articles appearing in this volume are the principal summarized results for long-form research articles. Readers seeking a more-detailed account of research activities are invited to seek out the primary materials appearing in print, detailed in the publications and presentations section at the end of this volume.

Highlights of research presented in this volume include:

- E. M. Campbell *et al.* summarize the present status and future plans for laser direct drive (p. 169).
- A. R. Christopherson *et al.* make the first direct measurements of the energy deposited by hot electrons into the DT fuel and its spatial distribution within the fuel. They also present a new technique to quantify the hot-electron preheat energy deposited into the dense DT fuel for all laser-fusion schemes (p. 172).
- W. Farmer *et al.* perform experiments using OMEGA’s state-of-the-art 4ω Thomson-scattering diagnostic to isolate the effect of heat transport using a directly driven, solid beryllium sphere. By comparing *LASNEX* simulations that included the Thomson probe beam, they found that the heat transport is being modeled correctly and that there are deficiencies in modeling other processes (p. 174).
- F. García-Rubio *et al.* investigate the effects of self-generated magnetic fields on the ablative Rayleigh–Taylor instability in the linear regimes. They find that the self-generated magnetic field significantly modifies the Rayleigh–Taylor dispersion relation even at small Mach numbers (p. 177).
- F. García-Rubio *et al.* study the Rayleigh–Taylor and Darrieus–Landau instabilities in an inertial confinement fusion context within the framework of the small critical-to-shell density ratio and weak acceleration regimes. This novel study includes non-isobaric effects and self-generated magnetic fields (p. 180).
- J. R. Davies *et al.* found that there are multiple magnetic-field advection terms that arise from the resistivity and electrothermal tensors in a magnetized plasma. Because these advection terms depend on significantly modified transport coefficients, the authors re-examined the well-established fits and summarize their findings (p. 183).
- H. Wen *et al.* study the convective gain and the kinetic inflation threshold for stimulated Raman scattering (SRS) driven by a broadband laser in an inhomogeneous plasma. They derive a formula that can predict when the convective SRS gain is enhanced and when the inflationary SRS threshold reaches a minimum (p. 186).
- A. L. Milder *et al.* present the first measurements of complete electron distributions without any assumptions on their shape or the underlying physics that produced them (p. 189).
- T. T. Simpson *et al.* introduce the “self-flying focus” (a nonlinear technique for spatiotemporal control), which produced an arbitrary trajectory intensity peak that can be sustained for distances comparable to the focal length and apply it to the generation of long plasma channels (p. 192).
- J. P. Palastro *et al.* report on the discovery of a novel regime of plasma wave excitation and wakefield acceleration that removes the wave-breaking limit, allowing for arbitrarily high electric fields. Laser-wakefield accelerators operating in this regime provide energy tunability independent of the plasma density and can accommodate large laser amplitudes (p. 195).
- S. Zhang *et al.* completed a comprehensive study of the equation of state of boron carbide (p. 198).
- V. Yu. Glebov *et al.* developed a neutron time-of-flight (nTOF) detector that can operate without a scintillator. The lack of a scintillator reduces the instrument response and makes it the fastest nTOF in use on OMEGA (p. 201).

- Z. L. Mohamed *et al.* extend the energy range of neutron detectors by interpolating the instrument response function (IRF) for neutrons of arbitrary energies, constructing an energy-dependent IRF, and then using a forward fit to apply that IRF (p. 205).
- C. Dorrer developed a framework to support optical parametric amplifier simulations using normalized equations and used that framework to study optical parametric amplification (OPA) operation with spectrally incoherent signals. Simulations are in agreement with the experimental demonstration of OPA with spectrally incoherent signals (p. 208).
- J. Lamoignon *et al.* compared laser-induced–damage thresholds of optical coatings at five well-equipped damage-testing facilities and find that the damage-testing results differ significantly between facilities (p. 211).
- M. S. Wei and S. F. B. Morse present summary information of the 12th Omega Laser Facility Users Group Workshop. Also presented are user Findings and Recommendations to the Omega Laser Facility (p. 214).
- J. Puth *et al.* summarize operations of the Omega Laser Facility during the fourth quarter of FY20 (p. 216).

Jessica L. Shaw
Editor

Direct-Drive Laser Fusion: Status, Plans, and Future

E. M. Campbell,¹ T. C. Sangster,¹ V. N. Goncharov,¹ J. D. Zuegel,¹ S. F. B. Morse,¹ C. Sorce,¹ G. W. Collins,¹ M. S. Wei,¹ R. Betti,¹ S. P. Regan,¹ D. H. Froula,¹ C. Dorrer,¹ D. R. Harding,¹ V. Gopalaswamy,¹ J. P. Knauer,¹ R. C. Shah,¹ O. M. Mannion,¹ J. A. Marozas,¹ P. B. Radha,¹ M. J. Rosenberg,¹ T. J. B. Collins,¹ A. R. Christopherson,¹ A. A. Solodov,¹ D. Cao,¹ J. P. Palastro,¹ R. K. Follett,¹ and M. Farrell²

¹Laboratory for Laser Energetics, University of Rochester

²General Atomics

Laser direct drive (LDD), along with laser indirect (x-ray) drive (LID) and magnetic drive with pulsed power, is one of the three viable approaches to achieving fusion ignition and gain in inertial confinement fusion (ICF). Here we summarize the present status and future plans for laser direct drive. The program is being executed on both the OMEGA laser at LLE and the National Ignition Facility (NIF) at Lawrence Livermore National Laboratory (LLNL). LDD research on OMEGA includes cryogenic implosions, fundamental physics including material properties, hydrodynamics, and laser–plasma interaction physics. LDD research on the NIF is focused on energy coupling and laser–plasma interaction physics at ignition-scale plasmas. Limited implosions on the NIF in the “polar-drive” configuration, where the irradiation geometry is optimized for LID, are also a feature of LDD research.

LDD implosions on OMEGA, developed by a data-based statistical model that employs machine learning, have achieved record performance and when hydrodynamically scaled to NIF energies would be predicted to produce fusion yields approaching a megajoule. Systematic experiments enabled by the high shot rate of OMEGA and advanced diagnostics to explore 3-D implosion performance are routinely fielded to understand degradation mechanisms that limit the fusion performance and to develop mitigation strategies.

Figures 1 and 2 show a comparison of the predicted D–T fusion yields compared to the data-based statistical model and the hydro-scaled performance assuming spherical irradiation conditions similar to OMEGA.

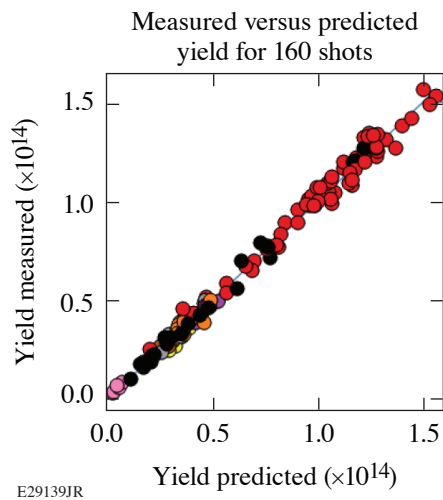


Figure 1

Comparison of a data-driven statistical model with actual experimental fusion yields. Over 160 experiments are well described by this predictive model with a wide range of parameters as described in the text.

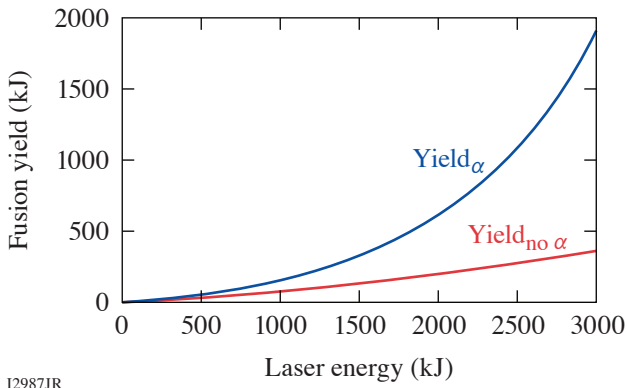
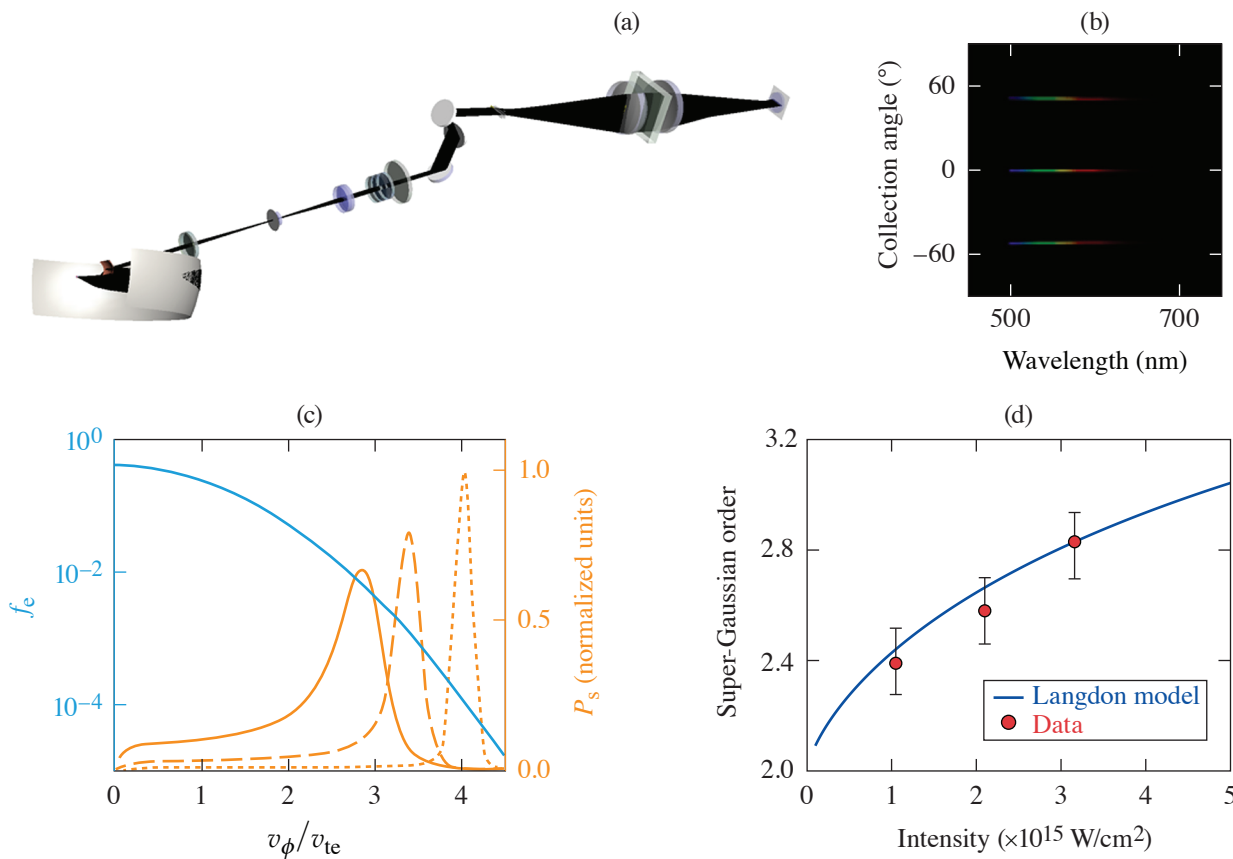


Figure 2
Fusion yield scaling with energy with and without alpha amplification.

I2987JR

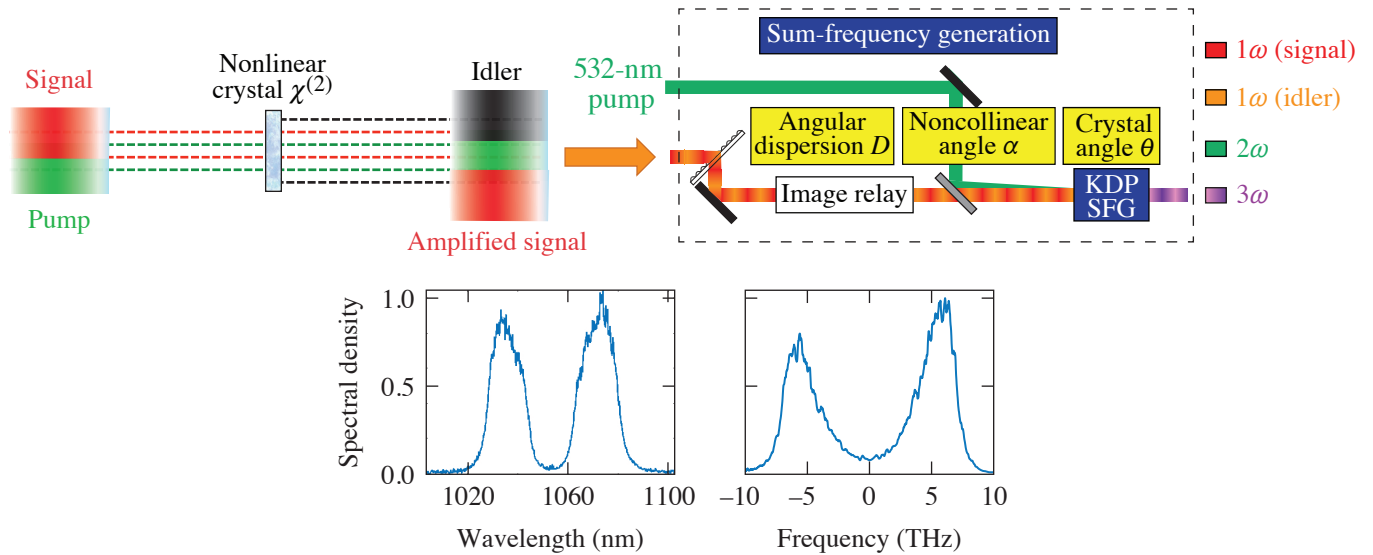
Laser–plasma interaction (LPI) physics continues to be a major focus of LDD research. Innovative diagnostics, for example, that measure electron distribution functions (EDF’s) on a single shot and increased laser/facility capabilities that enable a quantitative understanding of LPI over a range of plasma conditions created on both OMEGA and the NIF have advanced our understanding of LPI. The present state of research and future plans to eventually determine acceptable operating parameters and laser requirements for LDD ignition are summarized. Figure 3 shows an advanced optical Thomson-scattering diagnostic that enables one to determine the electron distribution function and the distortions in the EDF that occur with increasing laser intensity.



I2998JR

Figure 3
(a) Schematic and (b) Thomson-scattered light measured over 120°. (c) Scattered light from different angle select different regions of the electron distribution function. (d) Gaussian order of the electron distribution function’s dependence on laser intensity compared to the simulations.

All present major ICF facilities are based on laser science and technology developed decades ago. To increase the operating space for target designs, LLE has developed a concept for producing a broadband (bandwidth >10-THz) UV laser with a flexible pulse format. This concept, which leverages the science of optical parametric amplifiers and nonlinear frequency, has a goal of producing broadband (>10-THz) 350-nm light. The concept and early experiments that demonstrate the feasibility of the laser design are shown in Fig. 4. Demonstrating the laser at scale (100 J) and conducting experiments on both LPI suppression and laser imprint will be a major focus of LLE research in the years ahead.



I3001JR

Figure 4
Schematic of an advanced laser approach (sum-frequency generation) that exploits optical parametric amplifier technology to generate broadband (>1% bandwidth) UV light (the FLUX laser).

This material is based upon work supported by the Department of Energy National Nuclear Security Administration under Award Number DE-NA0003856, the University of Rochester, and the New York State Energy Research and Development Authority.

Direct Measurements of DT Fuel Preheat from Hot Electrons in Direct-Drive Inertial Confinement Fusion

A. R. Christopherson,^{1,2} R. Betti,^{1,2,3} C. J. Forrest,¹ J. Howard,^{1,2} W. Theobald,¹ J. A. Delettrez,¹ M. J. Rosenberg,¹ A. A. Solodov,¹ C. Stoeckl,¹ D. Patel,^{1,2} V. Gopalaswamy,^{1,2} D. Cao,¹ J. L. Peebles,¹ D. H. Edgell,¹ W. Seka,¹ R. Epstein,¹ M. S. Wei,¹ M. Gatu Johnson,⁴ R. Simpson,⁴ S. P. Regan,¹ and E. M. Campbell¹

¹Laboratory for Laser Energetics, University of Rochester

²Department of Mechanical Engineering, University of Rochester

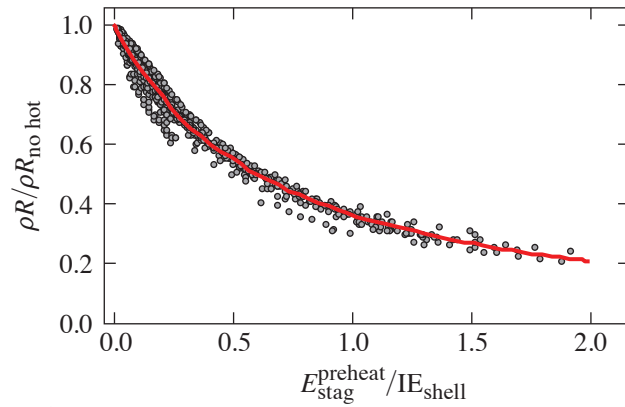
³Department of Physics and Astronomy, University of Rochester

⁴Massachusetts Institute of Technology

The generation of hot electrons from laser–plasma interactions has been a longstanding issue for inertial confinement fusion experiments since the early days of the field. Hot-electron preheat increases the entropy (adiabat) of the imploding shell, thereby degrading the final compression and quenching the ignition process. It is one of the major obstacles to ignition via laser direct drive. This summary describes the first direct measurement of the energy deposited by hot electrons into the DT fuel and its spatial distribution within the fuel. All previous attempts to measure preheat assessed only the conversion of laser energy into hot electrons. Since only a small fraction of the total hot-electron energy is deposited into the fuel, previous measurements could not be used to assess fuel preheat and areal-density degradation. This measurement is essential to understanding the effective adiabat (increased by preheat) of the imploding DT shell and the implosion performance. This important issue is addressed by presenting a new technique that can be used to quantify the hot-electron preheat energy deposited into the dense DT fuel for all laser-fusion schemes.

It is shown that, in direct-drive experiments, the hot-electron energy deposited in the DT fuel can be inferred by comparing the hard x-ray signals between a layered DT implosion and its mass-equivalent all-CH implosion irradiated with the same pulse shape. Since the hot-electron source is the same between the two implosions, the difference in hard x-ray signals is proportional to the preheat energy deposited in the DT layer. However, since a significant fraction of the ice layer is ablated during the implosion, it is important to also assess the preheat energy into the unablated fuel, which determines the final areal density. In Fig. 1, the relationship between the degradation in areal density due to preheat is plotted as a function of the preheat energy into the stagnated shell ($E_{\text{stag}}^{\text{preheat}}$) normalized to its internal energy (IE_{shell}) for a simulation ensemble of *LILAC* simulations of different targets. Estimating the areal-density degradation due to preheat therefore requires an additional model to describe the spatial distribution of the preheat energy within the fuel.

The spatial distribution of preheat energy was inferred in two experimental campaigns on OMEGA using warm CH targets with Cu-doped plastic payloads of varying thicknesses. The hard x rays from the Cu-doped plastic implosions were used to infer the hot-electron energy deposited in each layer. Post-shot analysis of the hard x-ray signals from these experiments confirmed that the electrons deposit their energy uniformly throughout the unablated mass. Therefore, the energy deposited into the unablated DT can be determined simply by calculating the energy deposited into all of the DT and multiplying by the unablated DT mass ratio. The final results, reported in Table I, show that the preheat analysis presented here explains the observed degradations in areal density with respect to their 1-D simulated values.



TC15340JR

Figure 1

Areal-density degradation versus preheat energy into the stagnated shell preheat ($E_{\text{stag}}^{\text{preheat}}$) normalized to the shell internal energy at peak velocity (IE_{shell}) for a large ensemble of *LILAC* simulations with preheat energies ranging from 0 to 100 J and design adiabats between 2 and 5.5. The red curve is the best fit to the simulation data.

 Table I: Areal-density (ρR) degradation for OMEGA DT-layered $\alpha \approx 4$ implosions.

Shot number	77064	85784	91830	91834
$E_{\text{DT}}^{\text{preheat}}$ (J)	13.0 ± 4.8	21.5 ± 7.1	$48. \pm 11.5$	40.5 ± 13.7
$E_{\text{stag}}^{\text{preheat}}$ (J)	4.9 ± 2.1	7.5 ± 2.5	15.0 ± 4.7	11.6 ± 3.9
IE_{shell} (J)	43.0	43.0	48.1	48.0
ρR_{exp} (mg/cm ²)	201 ± 17	154 ± 13	120 ± 9	127 ± 11
$\rho R_{\text{1-D}}$ (mg/cm ²)	225	186	184	188
ρR_{hs} (mg/cm ²)	190 ± 16	156 ± 13	124 ± 15	135 ± 155

The same technique is now being implemented at the National Ignition Facility (NIF) to measure preheat at megajoule laser energies and will be used to assess the viability of direct-drive designs, which may convert more laser energy into hot electrons as the size of the laser facility scales up. Quantifying how preheat scales from OMEGA to the NIF will have important implications for the design of direct-drive implosions on the NIF and the assessment of the next-generation inertial fusion facility. This technique also opens up new research avenues with respect to the design of direct-drive targets on OMEGA and, more specifically, the effects of different pulse shapes, ablator materials, and beam spot sizes on DT fuel preheat.

The authors thank Prof. D. Shvarts for many useful discussions. This material is based upon work supported by the Department of Energy National Nuclear Security Administration under Award Number DE-NA0003856, the University of Rochester, and the New York State Energy Research and Development Authority.

Validating Heat-Transport Models Using Directly Driven Spheres on OMEGA

W. Farmer,¹ G. Swadling,¹ J. Katz,² D. H. Edgell,² C. Bruulsema,³ M. Sherlock,¹ M. Rosen,¹ and W. Rozmus³

¹Lawrence Livermore National Laboratory

²Laboratory for Laser Energetics, University of Rochester

³University of Alberta

The indirect-drive approach to inertial confinement fusion (ICF) uses lasers to heat a radiation oven, or hohlraum. The radiation drive ablatively implodes a capsule filled with deuterium and tritium. Hohlräume are notoriously difficult to simulate due to the complex interplay of difficult-to-model physical processes. These processes include radiation and atomic physics, which generate the x-ray drive; laser–plasma interactions, which govern how the laser couples to the hohlraum; and heat transport, which determines how energy is partitioned. Further, integrated simulations of both a hohlraum and a capsule almost universally predict a capsule “bang time” earlier than observed, colloquially referred to as the “drive deficit.”^{1,2}

The hohlraum modeling framework has been developed over the years through simpler experiments, e.g., gold disk emission experiments,³ vacuum hohlraums,⁴ and gold sphere experiments.⁵ As a natural development of this effort, recent experiment and simulation work has been performed to isolate the effect of heat transport using a directly driven, solid beryllium sphere.⁶ These experiments were fielded on the OMEGA Laser System and utilized the state-of-the-art optical Thomson-scattering (OTS) and laser-coupling diagnostics. The OTS diagnostic precisely measured plasma conditions, and the laser coupling gave an accurate assessment of scattered laser energy, which is important for understanding the energy partition within the system. Comparisons to 2-D *LASNEX* simulations showed striking agreement with the data as long as certain heat-transport models were chosen.

The OTS measurements rely on the state-of-the-art fourth-harmonic Thomson-scattering diagnostic developed at LLE. Use of a 263-nm probe beam expands the range of accessible plasma conditions, enabling the study of high-density plasmas. This introduces technical challenges, however, because it places the spectrum in the ultraviolet range. Broadband imaging in this spectrum is notoriously difficult due to the limited number of transparent glass types available and their rapidly varying index of refraction. To overcome these issues, the Thomson-scattering diagnostic on OMEGA was upgraded in 2012 to a fully reflective optical system that delivers achromatic, diffraction-limited imaging performance across a broad spectral range.⁷ Two streak-camera–coupled spectrometers simultaneously record scattered light from fluctuations within the plasma, providing a highly resolved measurement of the complete Thomson-scattered spectrum. Improved spatial resolution allows one to precisely define the volume of plasma sampled, enabling the proper treatment of spatial gradients in the data analysis.

The Thomson-scattering technique allows experimenters to measure key parameters characterizing the experimental plasma, such as the density and temperature. Figure 1 shows the spectrum of scattered light that is determined by the underlying, thermally excited plasma fluctuations. To extract measurement of the plasma parameters, the recorded spectrum must be fitted using a theoretical model that describes the relative amplitudes and phase velocities of these fluctuations. Analysis is complicated by the presence of strong plasma emission and spatial gradients within the plasma. To produce accurate and consistent results, an improved fitting framework was developed that properly accounted for these effects. This resulted in precise, quantitative measurements of the temporal evolution of the plasma temperature and density, which can be directly compared to simulations.

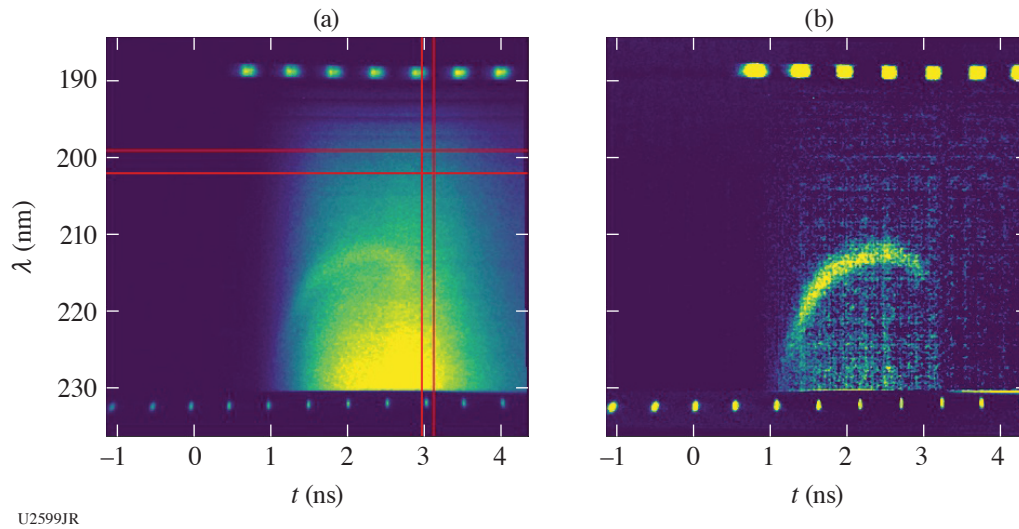


Figure 1
Scattered light observed by the OTS measurement. The vertical and horizontal axes correspond to time and wavelength, respectively: (a) with background and (b) with background subtracted. The bright spectral feature can be used to determine plasma conditions within the probe volume.

The uncoupled laser light was measured using the scattered-light calorimeters and spectrometers on OMEGA. The offline absolutely calibrated calorimeters give the total time-integrated uncoupled light, while the time-varying history of the unabsorbed light is recorded by the spectrometer streak camera. Multiple channels are averaged for each measurement. Two drive intensities were used (10^{14} W/cm² and 2.5×10^{14} W/cm²), and the diagnostics measured 3% and 10% scattered light for the low and high drive intensities, respectively.

Two-dimensional simulations that included the Thomson probe beam were performed in *LASNEX* using three commonly used heat-transport models as shown in Fig. 2. Remarkable agreement with the measurement is obtained with the nonlocal model (dashed curve in the plots), which agrees so well in panel (b) that the dashed curve is obscured by the measured data. Simulations

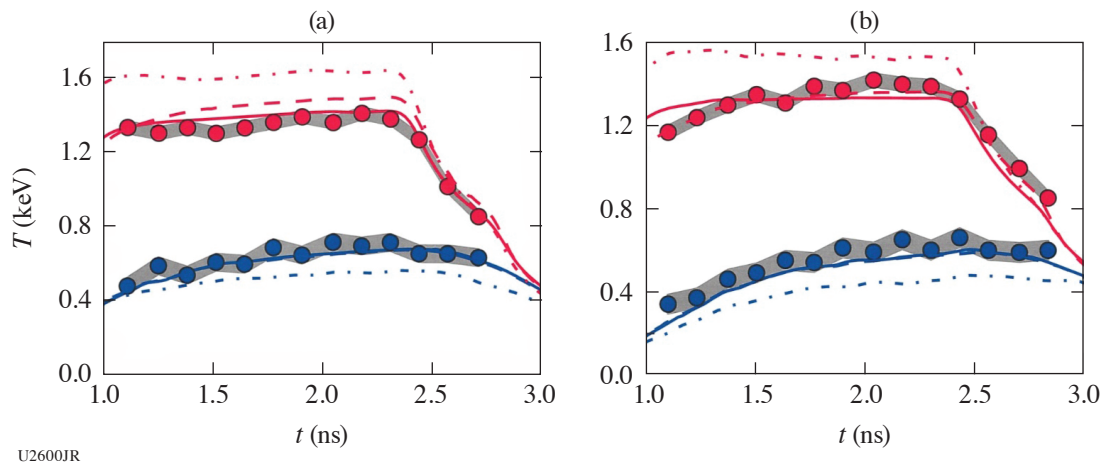


Figure 2
Comparisons of measured and simulated temperatures with nominal intensity of 2.5×10^{14} W/cm². (a) and (b) correspond to two different probe positions. Measurement is given by the circles, and the three models—a local heat-flux model, a nonlocal heat-transport model, and a restricted heat-flux model—are given by the solid, dashed, and dashed–dotted curves, respectively.

predicted that the scattered light was typically only 1% of the incident power, which does not match the measurement. The agreement with the plasma conditions suggests that heat transport is being modeled correctly and that deficiencies in modeling are in other processes. The understanding developed here is being applied to gold sphere experiments and will ultimately feed into progress toward a more-predictive hohlraum model.

This work was performed under the auspices of the U.S. Department of Energy by Lawrence Livermore National Laboratory under Contract DE-AC52-07NA27344.

1. R. P. J. Town *et al.*, *Phys. Plasmas* **18**, 056302 (2011).
2. O. S. Jones *et al.*, *Phys. Plasmas* **19**, 056315 (2012).
3. M. D. Rosen *et al.*, *Phys. Fluids* **22**, 2020 (1979).
4. R. E. Olson *et al.*, *Phys. Plasmas* **19**, 053301 (2012).
5. E. L. Dewald *et al.*, *Phys. Plasmas* **15**, 072706 (2008).
6. W. A. Farmer *et al.*, *Phys. Plasmas* **27**, 082701 (2020).
7. J. Katz *et al.*, *Rev. Sci. Instrum.* **83**, 10E349 (2012).

Magnetic-Field Generation and Its Effect on Ablative Rayleigh–Taylor Instability in Diffusive Ablation Fronts

F. García-Rubio,^{1,2} R. Betti,^{1,2,3} J. Sanz,⁴ and H. Aluie^{1,2}

¹Laboratory for Laser Energetics, University of Rochester

²Department of Mechanical Engineering, University of Rochester

³Department of Physics and Astronomy, University of Rochester

⁴Escuela Técnica Superior de Ingeniería Aeronáutica y del Espacio, Universidad Politécnica de Madrid

During the acceleration phase in direct-drive inertial confinement fusion (ICF), the Rayleigh–Taylor (RT) instability^{1–3} grows at the ablation front, degrading the integrity of the imploding shell. During the development of the RT instability, magnetic (B) fields are generated due to the misalignment of gradients of density and pressure, known as the baroclinic or Biermann battery effect.⁴ In the linear regime, the B field is coupled to the hydrodynamics mainly through the Righi–Leduc term. In essence, this term deflects the heat-flux lines, which in turn has a direct effect on the dynamics of these two instabilities (Fig. 1).

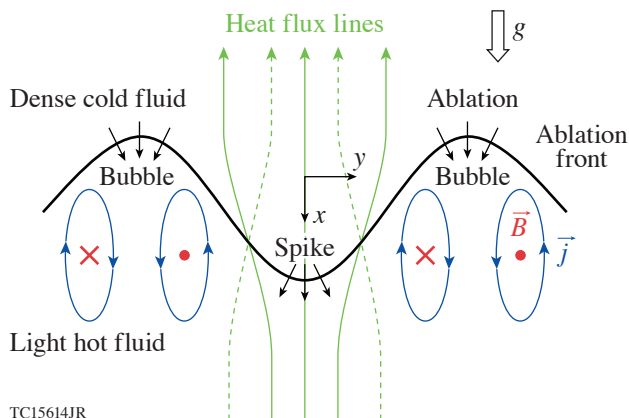


Figure 1

Sketch of the effect of the self-generated B fields on the RT instability. The magnetic field is generated by the Biermann battery effect and is perpendicular to the hydrodynamic motion. If the Righi–Leduc term causes the heat-flux lines to diverge from the spikes, then ablation is reduced and enhances the ablative RT instability (solid green lines with current \vec{j} and B-field sense as depicted). If the heat-flux lines converge, ablation increases, which contributes to stabilizing the RT instability (dotted lines and current \vec{j} and B-field sense opposite to the one depicted).

TC15614JR

In this summary, the effects of self-generated magnetic fields on the ablative RT instability are investigated in the linear regime. The main governing parameters are the Froude number (Fr), which stands for the ratio between ablative convection and acceleration of the target, and the Mach number at the ablation front (Ma), assumed to be small (isobaricity). When normalized, the Righi–Leduc term is proportional to $c_R \text{Ma}^2$, with c_R being a constant of order unity.

The results for the hydrodynamics coupled to the magnetic field are compared to the uncoupled case in Fig. 2. For small wave numbers, the dispersion relation is similar to the RT instability of immiscible fluids with Atwood number equal to unity, $\gamma \sqrt{kg}$. Ablation stabilization becomes effective for larger wave numbers until the RT instability is suppressed at a certain cutoff k_c . The cutoff wavelength decreases at larger Froude numbers.

The self-generated B field significantly modifies the dispersion relation even for small Mach numbers. Its effect becomes important when ablation stabilization takes place (near the maximum of the spectrum). It is not monotonic and can either enhance or stabilize the RT instability depending on the Froude number. For $\text{Fr} = 1$, the self-generated B field plays a destabilizing role and

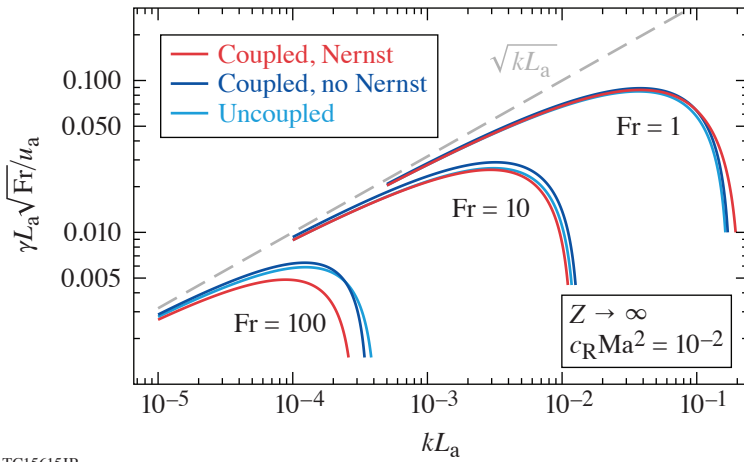


Figure 2
Dispersion relation for different Froude numbers. Light blue curves: hydrodynamics uncoupled from induction; dark blue curves: hydrodynamics and induction coupled, $c_R Ma^2 = 10^{-2}$, without Nernst; red curves: hydrodynamics and induction coupled, $c_R Ma^2 = 10^{-2}$, with Nernst. The large atomic number $Z \rightarrow \infty$ is considered, and the magnetic Reynolds number is infinite.

TC15615JR

enlarges the region of unstable modes. This effect is greatly amplified by the Nernst term, notably close to the cutoff. For $Fr = 10$, however, the stabilizing character of the B field switches when the Nernst term is considered, shortening the range of unstable modes k . This transition in the stabilizing character is completed in the case $Fr = 100$, where the self-generated B field shortens the range of unstable modes in cases both with and without Nernst. In the former case, this effect is especially pronounced since the cutoff is reduced by almost 40%.

An interesting feature observed is that, when the Nernst term is considered, the stabilizing character of the B field is maintained for a given Froude number. Therefore, a Fr threshold exists that depends exclusively on Z for which the stabilizing character of the B field switches. This is shown in Fig. 3, where the difference in growth ratio is shown for the most-unstable mode for every Froude number. The dependence of threshold Fr on Z is rather weak since we obtained $Fr = 6, 5,$ and 3.4 for $Z = 1, 4,$ and ∞ , respectively. Although this figure is shown for $Ma \sim 10^{-1}$, the same threshold Fr is obtained when varying the Mach number.

The effect of magnetic diffusivity is shown in Table I, where the computed coefficient measures the similarity of the growth rate to the pure hydrodynamic case (close to 0) or to the perfectly conductive case (close to 1). It can be seen that for $Fr = 1$ the

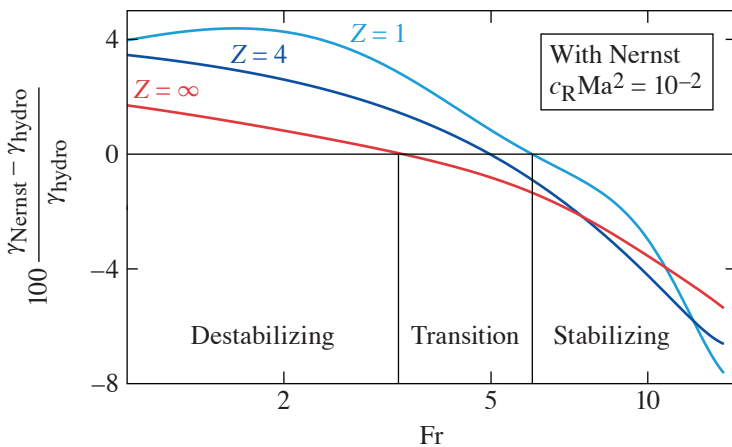


Figure 3
Difference in growth rate (computed as a percentage) between the uncoupled (γ_{hydro}) and coupled with Nernst (γ_{Nernst}) cases. For every Froude number, the most-unstable mode, maximum γ_{hydro} is chosen.

TC15616JR

system is very sensitive to the magnetic Reynolds number. Ablation fronts in ICF tend to be very diffusive, and Re_m is usually low. Therefore, the effect of the B field on perturbations whose wavelengths are comparable to the ablation front length scale is suppressed by resistivity. Contrary to this behavior, long-wavelength perturbations are insensitive to Re_m , as can be seen for the case $Fr = 10$. At this Froude number, unstable perturbations penetrate deep into the hot conductive plasma, and the effect of the B field (which, for these perturbations is stabilizing) is unaltered by diffusion.

Table I: Coefficient $\gamma - \gamma|_{\text{hydro}} / \gamma|_{\text{Nerst}} - \gamma|_{\text{hydro}}$. Case considered: $Z \rightarrow \infty$ and $Ma = 0.1$.

	$Re_m = 10^{-2}$	$Re_m = 10^{-1}$	$Re_m = 1$	$Re_m = 10$
$Fr = 1, k = 10^{-1}$	0.076	0.28	0.62	0.97
$Fr = 10, k = 5 \times 10^{-3}$	1.16	1.19	1.18	1.13

This work is supported by the Department of Energy Office of Science, Fusion Energy Sciences program grants DE-SC0016258 and DE-SC0014318. H. Aluie was also supported by DOE grants DE-SC0020229 and DE-SC0019329; NASA grant 80NSSC18K0772; and NNSA grants DE-NA0003856 and DE-NA0003914. This material is based upon work supported by the Department of Energy National Nuclear Security Administration under Award Number DE-NA0003856, the University of Rochester, and the New York State Energy Research and Development Authority.

1. S. E. Bodner, Phys. Rev. Lett. **33**, 761 (1974).
2. H. J. Kull, Phys. Fluids B **1**, 170 (1989).
3. H. Takabe *et al.*, Phys. Fluids **28**, 3676 (1985).
4. K. Mima, T. Tajima, and J. N. Leboeuf, Phys. Rev. Lett. **41**, 1715 (1978).

Self-Consistent Theory of the Darrieus–Landau and Rayleigh–Taylor Instabilities with Self-Generated Magnetic Fields

F. García-Rubio,^{1,2} R. Betti,^{1,2,3} J. Sanz,⁴ and H. Aluie^{1,2}

¹Laboratory for Laser Energetics, University of Rochester

²Department of Mechanical Engineering, University of Rochester

³Department of Physics and Astronomy, University of Rochester

⁴Escuela Técnica Superior de Ingeniería Aeronáutica y del Espacio, Universidad Politécnica de Madrid

The Rayleigh–Taylor instability (RT) has been thoroughly studied in the context of inertial confinement fusion (ICF).^{1,2} In the weak acceleration regime, the cutoff wavelength is large compared to the ablation-front scale length, $k_{c0}L_a \ll 1$, and the dispersion relation can be analytically derived by exploiting the sharp-boundary model (SBM).^{3,4} In the limit of zero acceleration, sufficiently long wavelengths undergo another type of instability known as Darrieus–Landau (DL). This instability is generic for fronts where a dense fluid expands into a lighter one, as typically occurs in flames.^{5,6} During the development of these instabilities, magnetic (B) fields are generated due to the misalignment of gradients of density and pressure, known as baroclinic or the Biermann battery effect.⁷ In the linear regime, the B field is coupled to the hydrodynamics mainly through the Righi–Leduc term. In essence, this term deflects the heat-flux lines, which in turn has a direct effect on the dynamics of these two instabilities.

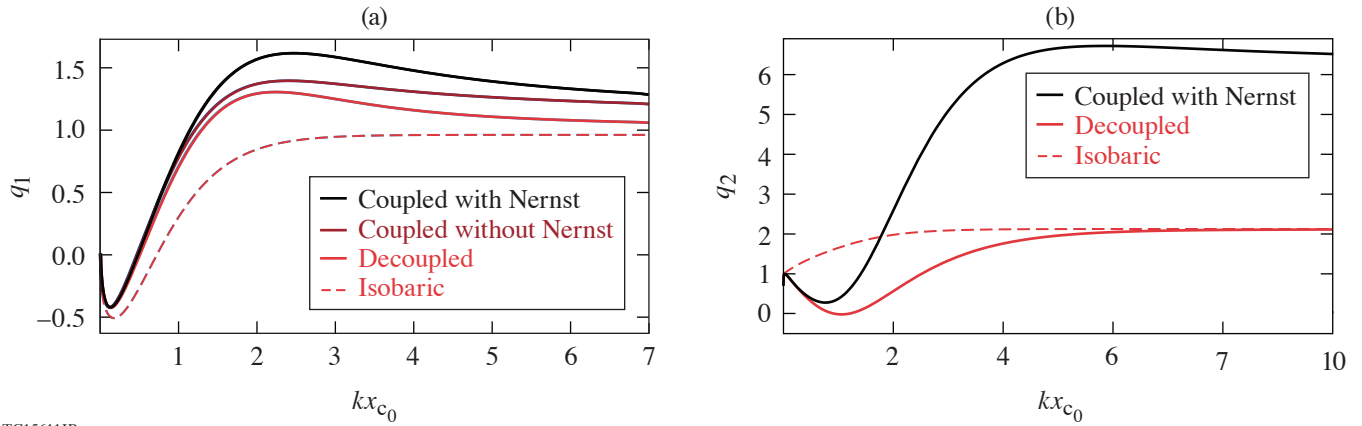
In this summary, the Rayleigh–Taylor and Darrieus–Landau instabilities are studied in an ICF context within the framework of a small critical-to-shell density ratio D_R and a weak acceleration regime, i.e., large Froude number $Fr \gg 1$. This number stands for the ratio between ablative convection and the acceleration of the capsule. The two main novelties in this study are the inclusion of non-isobaric effects and the self-generated magnetic fields. The use of an SBM leads to a single analytical expression of the dispersion relation encompassing both instabilities:

$$\gamma = \frac{u_a}{L_a} \sqrt{\frac{kL_a}{Fr} - \frac{q_1(kL_a)^{8/5}}{\text{perturbed pressure}} - \frac{1+f_1+q_2}{2}ku_a} \quad , \quad (1)$$

where u_a is the ablation velocity at the ablation front. The eigenvalues $\{f_i, q_i\}$ correspond to the perturbed mass and momentum fluxes through the ablation front, and $i = 1, 2$ refers to its quasi-steady and nonstationary values, respectively. They depend only on the perturbation wavelength normalized with the conduction layer width, $kx_{c0} = 0.0117kL_a(2n_a/n_c)^{5/2}$ and are shown in Fig. 1.

For $kx_{c0} > 0.5$, the overpressure generated at the spikes q_1 is positive and becomes the main damping mechanism. For $kx_{c0} < 0.5$, q_1 is negative (underpressure) and destabilizing, becoming the driving mechanism of the DL instability. Asymptotic analysis allows one to derive the scaling laws of the underpressure for a small wave number. The non-isobaric effects play an important role for these perturbations, making q_1 scale as $q_1 = -5.8(kx_{c0})^{11/15}$, compared to the isobaric case studied in Ref. 6, where $q_1 = -(5kx_{c0}/2)^{2/5}$.

Under the assumptions of the sharp boundary model, the effect of the self-generated magnetic field is always stabilizing. It increases both the momentum and mass fluxes. The Nernst convection enhances the stabilizing effect of the B field. For perturbation wavelengths longer than the distance between ablation front and critical surface, $kx_{c0} < 1$, the B field is less effective, becoming



TC15611JR

Figure 1

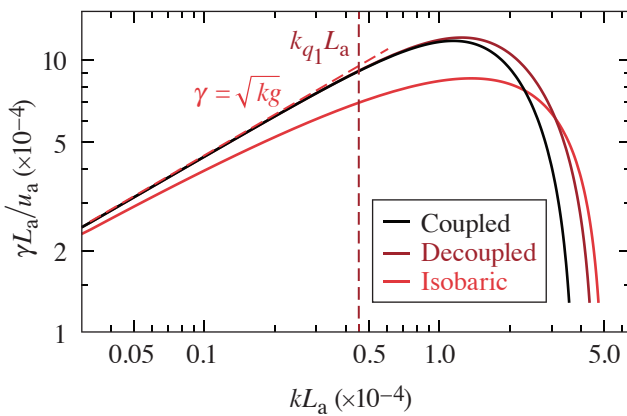
Eigenvalues (a) q_1 and (b) q_2 (quasi-steady and nonsteady perturbed momentum flux). Black solid curve: coupled with Nernst; maroon solid curve: coupled without Nernst; red solid curve: B field decoupled; red dashed curve: results from the isobaric model in Ref. 6.

totally negligible in the DL instability region. The B-field effect is significantly stronger on the unsteady momentum flux q_2 . This has an important effect on the convective stabilization term in Eq. (1), which is enhanced from “ $-2ku_a$ ” to “ $-4ku_a$ ”

The analysis of the dispersion relation reveals that the combination

$$D_R Fr^{2/3} = 0.015 \frac{\left(\frac{u_a}{1 \mu\text{m/ns}}\right)^4 \left(\frac{n_a}{10^{24} \text{cm}^{-3}}\right)^{2/3}}{\left(\frac{g}{100 \mu\text{m/ns}^2}\right)^{2/3} \left(\frac{T_a}{10 \text{eV}}\right)^{8/3}} \quad (2)$$

dictates the behavior of the spectrum. For $D_R Fr^{2/3} \ll 1$, it is well described by the ablative RT instability in the isobaric regime, and the cutoff takes place for $kL_a \approx Fr^{-5/3}$. In the opposite limit, $D_R Fr^{2/3} \gg 1$, two regions can be defined. The long perturbations with $kL_a < D_R^{11/8} / Fr^{3/4}$ undergo RT instability, while the part of the spectrum with $kL_a < D_R^{11/8} / Fr^{3/4}$ is DL dominated. In this limit, the cutoff becomes independent of the Froude number: $kL_a \approx 7.6 D_R^{5/2}$. The regime of application for ICF corresponds to $D_R Fr^{2/3} \lesssim 1$. When this parameter is close to unity, the DL effect operates by reducing the restoring overpressure and increasing the wave number at which ablation comes into play. It is precisely in this range, $D_R Fr^{2/3} \sim 1$, where the effect of the self-generated B fields becomes more important. They enhance the stabilizing effect of ablation and can significantly reduce the cutoff. A configuration of interest for ICF is shown in Fig. 2.



TC15612JR

Figure 2

Dispersion relation for $u_a = 1.2 \mu\text{m/ns}$, $T_a = 7.5 \text{eV}$, $n_a = 10^{24} \text{cm}^{-3}$, and $g = 50 \mu\text{m/ns}^2$, which gives $Fr = 50$ and $D_R Fr^{2/3} = 0.11$. Black curve: magnetic fields and non-isobaric effects are included; maroon curve: non-isobaric effects are included, but the hydrodynamic is decoupled from induction; red curve: RT instability under the isobaricity assumption. The wave number where the perturbed pressure q_1 becomes positive is $k_{q_1} L_a = 4.4 \times 10^{-5}$.

A schematic of the different regimes supported in Eq. (1) is plotted in Fig. 3. In this schematic, the stability of a generic perturbation with wave number kL_a is given as a function of the Froude number and the critical- to shell-density ratio. It must be understood from an asymptotic analysis point of view; consequently, the transition from one region to another is blurry rather than a well-defined curve.

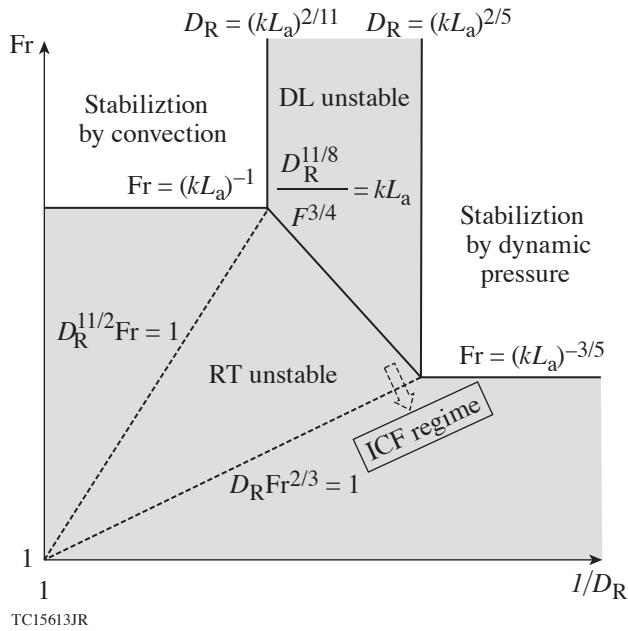


Figure 3
Schematic of the behavior of a given perturbation wave number kL_a as a function of the Froude number (Fr) and critical- to shell-density ratio D_R . The ICF regime corresponds to $D_R Fr^{2/3} \leq 1$.

This work is supported by the Department of Energy Office of Science, Fusion Energy Sciences program grants DE-SC0016258 and DE-SC0014318. H. Aluie was also supported by DOE grants DE-SC0020229, DE-SC0019329, NASA grant 80NSSC18K0772, and NNSA grants DE-NA0003856, DENA0003914. This material is based upon work supported by the Department of Energy National Nuclear Security Administration under Award Number DENA0003856, the University of Rochester, and the New York State Energy Research and Development Authority.

1. H. J. Kull, Phys. Fluids B **1**, 170 (1989).
2. H. Takabe *et al.*, Phys. Fluids **28**, 3676 (1985).
3. J. Sanz, Phys. Rev. Lett. **73**, 2700 (1994).
4. V. N. Goncharov *et al.*, Phys. Plasmas **3**, 1402 (1996).
5. P. Clavin and L. Masse, Phys. Plasmas **11**, 690 (2004).
6. J. Sanz, L. Masse, and P. Clavin, Phys. Plasmas **13**, 102702 (2006).
7. K. Mima, T. Tajima, and J. N. Leboeuf, Phys. Rev. Lett. **41**, 1715 (1978).

Transport Coefficients for Magnetic-Field Evolution in Inviscid Magnetohydrodynamics

J. R. Davies,¹ H. Wen,¹ J.-Y. Ji,² and E. Held²

¹Laboratory for Laser Energetics, University of Rochester

²Department of Physics, Utah State University

In a magnetized plasma, the resistivity and electrothermal coefficient become tensors. Transport differs parallel and perpendicular to the magnetic field; when transport perpendicular to both the conventional direction of transport and the magnetic field occurs, it is called “cross-field transport.” Braginskii¹ expressed the resulting Ohm’s law in the form

$$\begin{aligned} \vec{E} = & -\vec{v} \times \vec{B} + \frac{\vec{j}}{n_e e} \times \vec{B} - \frac{\nabla P_e}{n_e e} \\ & + \frac{\eta_{\parallel}}{\varepsilon_0 \omega_{pe}^2 \tau_{ei}} \vec{b}(\vec{b} \cdot \vec{j}) + \frac{\eta_{\perp}}{\varepsilon_0 \omega_{pe}^2 \tau_{ei}} \vec{b} \times (\vec{j} \times \vec{b}) - \frac{\eta_{\wedge}}{\varepsilon_0 \omega_{pe}^2 \tau_{ei}} (\vec{b} \times \vec{j}) \\ & - \beta_{\parallel} (\vec{b} \cdot \nabla T_e) - \beta_{\perp} \vec{b} \times (\nabla T_e \times \vec{b}) - \beta_{\wedge} (\vec{b} \times \nabla T_e), \end{aligned} \quad (1)$$

where v is ion velocity (m s^{-1}), B is magnetic field (T), j is current density (A m^{-2}), n_e is electron density (m^{-3}), e is electron charge (C), P_e is electron pressure (Pa), ε_0 is the permittivity of free space (F m^{-1}), ω_{pe} is electron plasma frequency (s^{-1}), τ_{ei} is electron–ion collision time (s), b is a unit vector in the direction of the magnetic field, T_e is electron temperature (eV), η is a dimensionless resistivity coefficient, β is a dimensionless electrothermal coefficient, \parallel indicates parallel, \perp indicates perpendicular, and \wedge indicates cross. Electron viscosity has been neglected for simplicity. The only contributions the magnetized transport coefficients make to magnetohydrodynamics (MHD) are to modify magnetic-field evolution, given by $\nabla \times E$, and Ohmic heating, given by $j \cdot E$. The resulting expression for magnetic-field evolution is long and obscures the physical significance of the transport terms. Using vector identities, the equation can be rearranged into several different forms that are more compact and have terms with a clear physical interpretation.² The most compact form is

$$\begin{aligned} \frac{\partial \vec{B}}{\partial t} = & \nabla \beta_{\parallel} \times \nabla T_e + \frac{\nabla P_e \times \nabla n_e}{n_e^2 e} + \nabla \times (\vec{v}_{\text{eff}} \times \vec{B}) + \vec{v}_{\eta} \times (\nabla \times \vec{B}) + \eta_{\parallel} \frac{\delta_e^2}{\tau_{ei}} \nabla^2 \vec{B}, \\ \vec{v}_{\text{eff}} = & \vec{v} - \frac{\vec{j}}{n_e e} \left(1 + \frac{\eta_{\wedge}}{\chi_e} \right) - \frac{\eta_{\perp} - \eta_{\parallel}}{\chi_e} \frac{\vec{b} \times \vec{j}}{n_e e} - \frac{\beta_{\wedge}}{\chi_e} \frac{e \tau_{ei}}{m_e} \nabla T_e + \frac{\beta_{\parallel} - \beta_{\perp}}{\chi_e} \frac{e \tau_{ei}}{m_e} \nabla T_e \times \vec{b}, \\ \vec{v}_{\eta} = & -\nabla \left(\eta_{\parallel} \frac{\delta_e^2}{\tau_{ei}} \right), \delta_e = \frac{c}{\omega_{pe}}, \end{aligned} \quad (2)$$

where $\chi_e = eB\tau_{ei}/m_e$ is the electron Hall parameter, a dimensionless measure of the strength of magnetization compared to collisions. In this form, the transport coefficients are seen to lead to a magnetic-field source term $\nabla \beta_{\parallel} \times \nabla T$, advection of mag-

netic field with electron transport, seen in the terms dependent on j and ∇T_e in the effective velocity v_{eff} , advection of magnetic field to regions of lower resistivity from v_η , and magnetic diffusion. These physical effects are present in whatever mathematical form is chosen. Haines³ attributes the advection terms to electron heat flux, which has terms in j as well as ∇T_e , describing the magnetic field as being frozen to the electrons responsible for thermal transport, not the bulk fluid, due to their lower collision frequency. In this analogy, the η_\wedge/χ_e term arises from perpendicular electrothermal heat flux, the $(\eta_\perp - \eta_\parallel)/\chi_e$ term from cross-field electron heat flux, the β_\wedge/χ_e term from perpendicular thermal conduction, and the $(\beta_\parallel - \beta_\perp)/\chi_e$ term from cross-field thermal conduction.

The advection terms in the effective velocity depend on modified transport coefficients that have not been explicitly considered in determining fits for the transport coefficients, motivating a reconsideration of these fits. We examined the fits given by Braginskii,¹ Epperlein and Haines,⁴ and Ji and Held.⁵ The transport coefficients are obtained by solving the Fokker–Planck equation in the limit of small mean free path and collision time. Braginskii used a third-order expansion in Laguerre polynomials and gives fits in χ_e for effective atomic numbers $Z = 1, 2, 3, 4$, and $Z \rightarrow \infty$ (no electron–electron collisions) stated to be within 20% of the approximate solutions. Braginskii’s fits have incorrect limiting forms for η_\wedge and β_\perp as $\chi_e \rightarrow \infty$ and do not adequately constrain the values for $Z > 4$, but are still widely used. Epperlein and Haines used a direct numerical solution and give fits in χ_e for $Z = 1, 2, 3, 4, 5, 6, 7, 8, 10, 12, 14, 20, 30, 60$, and $Z \rightarrow \infty$ accurate to within 15%. While Epperlein and Haines’ results do allow a more-accurate interpolation of the coefficients for arbitrary Z than Braginskii’s, their fitting parameters for η_\perp , η_\wedge , and β_\perp are discontinuous in Z , so they can give physically incorrect gradients in these coefficients due to variations in Z , which will affect magnetic-field advection. Epperlein and Haines’ fits are perhaps the most widely used in MHD codes. Ji and Held used the expansion in Laguerre polynomials, increasing the number of terms until the coefficients changed by less than 1%, which required up to 160 terms. They give fits in χ_e and Z , valid for any Z from 0 to 100, accurate to better than 1%, making them the most convenient and accurate set of fits of which we are aware. It is important to note that the stated fitting accuracies do not apply to the modified coefficients appearing in the effective velocity.

For the modified transport coefficients, Braginskii’s incorrect limiting forms for η_\wedge and β_\perp as $\chi_e \rightarrow \infty$ are irrelevant. All three fits give $1 + \eta_\wedge/\chi_e \rightarrow 1$ and $(\beta_\parallel - \beta_\perp)/\chi_e \rightarrow \beta_\parallel/\chi_e$ as $\chi_e \rightarrow \infty$. There is good agreement on β_\parallel and η_\parallel . The fits for $1 + \eta_\wedge/\chi_e$ agree to better than 5%. There is also good agreement on β_\wedge/χ_e , which determines the Nernst velocity, except at small Hall parameters (< 2) where Braginskii underestimates this term by up to 10%, which can be physically significant. Serious issues arise with the $(\eta_\perp - \eta_\parallel)/\chi_e$ and $(\beta_\parallel - \beta_\perp)/\chi_e$ terms, where both Epperlein and Haines and Ji and Held give physically incorrect results for $\chi_e \rightarrow 0$, as can be seen in Fig. 1. These modified transport coefficients represent cross-field transport of the magnetic field so they should be proportional to χ_e as $\chi_e \rightarrow 0$. Epperlein and Haines give quite the opposite behavior with a peak in both coefficients at $\chi_e < 1$, which increases with Z . Ji and Held’s fits fail to go to zero as $\chi_e \rightarrow 0$, the error being most significant for $(\beta_\parallel - \beta_\perp)/\chi_e$, which goes negative and becomes increasingly negative as Z increases. Only Braginskii gives physically accurate results. Since Epperlein and Haines and Ji and Held are accurate for sufficiently large Hall parameters, we can see that Braginskii’s $(\eta_\perp - \eta_\parallel)/\chi_e$ is a significant overestimate for moderate Hall parameters; it also has a nonphysical double hump.

To evaluate the accuracy of the fits for these modified coefficients, we obtained $(\beta_\perp - \beta_\parallel)/\chi_e$ from a direct numerical solution of the Fokker–Planck equation using the code *OSHUN*,⁶ which is shown as squares in Fig. 1(a). Braginskii is the most accurate for Hall parameters close to zero, but Ji and Held rapidly give the most-accurate fit as the Hall parameter increases. We also compared the fits for the Nernst term β_\wedge/χ_e to the *OSHUN* results and found that Ji and Held’s fit is the most accurate. For the $(\eta_\perp - \eta_\parallel)/\chi_e$ term, we used the results directly from Ji and Held’s 320-term solution, shown as squares in Fig. 1(b), which again shows that Braginskii is the most accurate for Hall parameters close to zero, but Ji and Held rapidly give the most-accurate fit as the Hall parameter increases. Since none of the fits are accurate for $(\eta_\perp - \eta_\parallel)/\chi_e$ and $(\beta_\parallel - \beta_\perp)/\chi_e$, we tried fitting the direct calculations of these coefficients shown in Fig. 1 with a function of χ_e and Z based on those used by Ji and Held. The fits are too long to be included in this summary but can be found elsewhere.²

In conclusion, we have found that there are multiple magnetic-field advection terms that arise from the resistivity and electrothermal tensors in a magnetized plasma. These advection terms depend on significantly modified transport coefficients, which

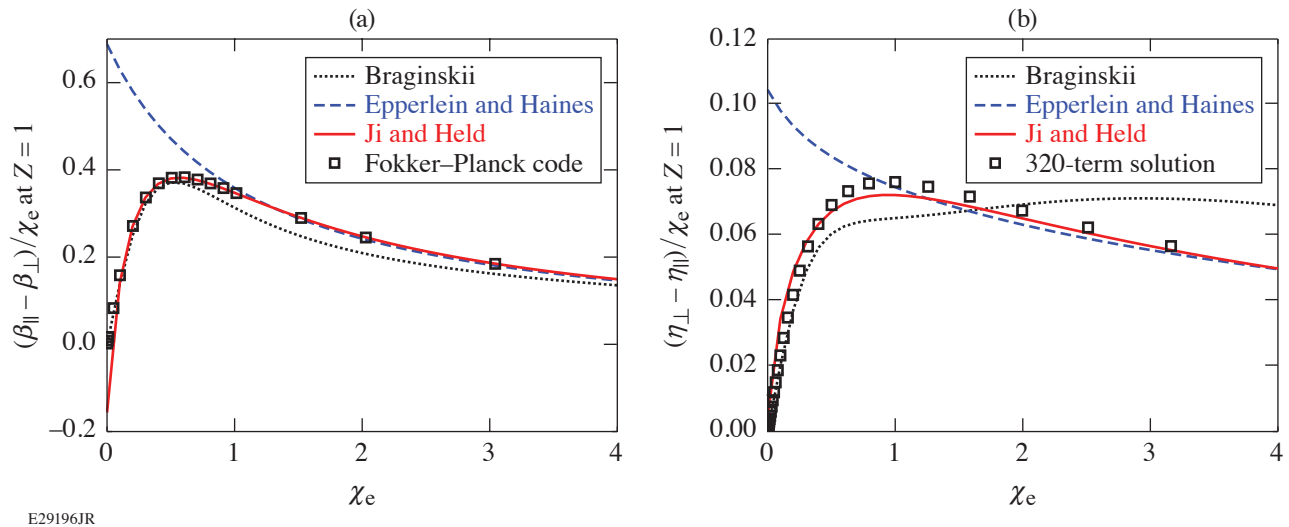


Figure 1

Modified (a) electrothermal and (b) resistivity coefficients that determine cross-field advection of magnetic field at $Z = 1$. Fits from Braginskii, Epperlein and Haines, and Ji and Held are shown as curves, and direct solutions from (a) the Fokker-Planck code *OSHUN* and (b) Ji and Held's 320-term expansion are shown as squares.

motivated a reconsideration of well-established fits. Braginskii's fits were found to be more accurate than expected, with the only significant error being an overestimate in advection due to perpendicular resistivity at intermediate Hall parameters. It is also worth noting that Braginskii underestimates the Nernst velocity by up to 10% at small Hall parameters. Epperlein and Haines' fits give physically incorrect results for advection due to perpendicular resistivity and perpendicular electrothermal coefficient, greatly overestimating these effects for Hall parameters < 1 . It is also worth noting that Epperlein and Haines' fits for perpendicular resistivity show significant discontinuities in their variation with Z . Ji and Held's fits give physically incorrect results for advection due to perpendicular resistivity and perpendicular electrothermal coefficient, but the errors are only significant near the zero Hall parameter. Ji and Held's fits are the only ones considered that are continuous functions of Z , valid from 0 to 100. New fits have been obtained,² following Ji and Held's approach, that give significantly improved accuracy for magnetic-field advection.

This material is based upon work supported by the Department of Energy National Nuclear Security Administration under Award Number DE-NA0003856, the University of Rochester, and the New York State Energy Research and Development Authority.

1. S. I. Braginskii, in *Reviews of Plasma Physics*, edited by M. A. Leontovich (Consultants Bureau, New York, 1965), Vol. 1, p. 205.
2. J. R. Davies *et al.*, "Transport Coefficients for Magnetic-Field Evolution in Inviscid Magnetohydrodynamics," submitted to *Physics of Plasmas*.
3. M. G. Haines, *Plasma Phys. Control. Fusion* **28**, 1705 (1986).
4. E. M. Epperlein and M. G. Haines, *Phys. Fluids* **29**, 1029 (1986).
5. J.-Y. Ji and E. D. Held, *Phys. Plasmas* **20**, 042114 (2013).
6. M. Tzoufras *et al.*, *Phys. Plasmas* **20**, 056303 (2013).

Kinetic Inflation of Convective Raman Scattering Driven by a Broadband, Frequency-Modulated Laser Pulse

H. Wen,¹ R. K. Follett,¹ A. V. Maximov,¹ D. H. Froula,¹ F. S. Tsung,² and J. P. Palastro¹

¹Laboratory for Laser Energetics, University of Rochester

²Department of Physics and Astronomy, University of California, Los Angeles

Stimulated Raman scattering (SRS), a process in which a light wave decays into a plasma wave and another light wave, can reduce laser absorption by scattering light away from the target. SRS can also generate hot electrons that preheat the fusion fuel in the direct-drive inertial confinement fusion (ICF) scheme, making fuel compression more difficult. Inflationary SRS (iSRS) occurs in the kinetic regime when the electron velocity distribution is flattened due to electron trapping. The flattening of the electron distribution not only reduces the Landau damping rate but also decreases the plasma wave frequency, leading to an SRS reflectivity much higher than what is predicted by the convective SRS gain model¹ for a Maxwellian velocity distribution. In this work, we study the convective gain and the kinetic inflation threshold for SRS driven by a broadband laser in an inhomogeneous plasma using the particle-in-cell (PIC) code *OSIRIS*. Based on the cancellation of the bandwidth effect and the spatial detuning effect, we derived a simple formula that can predict when the convective SRS gain is enhanced and when the iSRS threshold reaches a minimum. The analytic formula is consistent with the PIC simulation results over a broad range of parameter space.

The frequency of a pump with a sinusoidal phase modulation can be written as $\omega_0(x, t) = \bar{\omega}_0 + \omega_m \delta \sin(\omega_m t - x\omega_m/c)$, where $\bar{\omega}_0$ is the central frequency of the pump and $\omega_m(\delta)$ is the phase modulation frequency (depth). The bandwidth of this broadband pump is defined as $\Delta\omega = 2\omega_m\delta/\pi$. If SRS is driven by a broadband laser in an inhomogeneous plasma, SRS resonance (the location where the frequency mismatch is close to zero) moves in time. When the SRS resonance follows the trajectory of the SRS scattered light, i.e.,

$$\xi \equiv \frac{\Delta\omega\omega_m}{\bar{\omega}_0^2} = \frac{\omega_p}{8\bar{\omega}_0 k_0 L_n}, \quad (1)$$

where ω_p is the local plasma frequency, k_0 is the laser wave vector, and L_n is the density scale length, the SRS amplification is greatly enhanced.

Figure 1 shows that the condition for achieving the peak convective amplification depends on neither the temperature T_e nor the laser bandwidth $\Delta\omega$ (or the modulation frequency ω_m) alone. The convective gains in the fluid (open symbols) and kinetic (solid symbols) regimes for various bandwidths are normalized to the respective Rosenbluth gains,¹ 1.67 (fluid regime) and 1.14 (kinetic regime). As a reference, two runs with zero bandwidth (denoted as “ $\Delta\omega = 0$ ”) were carried out and their convective gains are shown as stars in Fig. 1. The Rosenbluth theory is well recovered by the zero-bandwidth simulation in the fluid regime. In both the fluid ($T_e = 0.1$ keV) and kinetic ($T_e = 2$ keV) regimes and for all bandwidths, the convective gains increase as ξ increases, peaking near the value of ξ predicted by Eq. (1), and then decreasing back to the level at $\xi = 0$.

Because iSRS depends on the plasma wave amplitude, one would expect the iSRS threshold to decrease when the maximum convective gain is enhanced. Accordingly, the iSRS threshold is expected to reach its minimum value when the maximum-gain condition [Eq. (1)] is satisfied. We carried out 1-D PIC simulations of self-seeded SRS in the kinetic regime to examine this hypothesis.

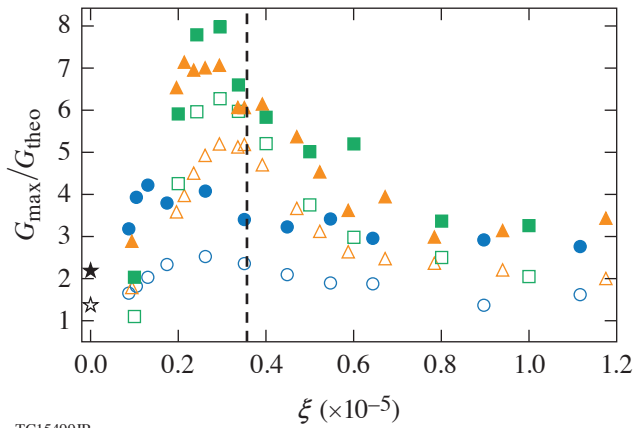
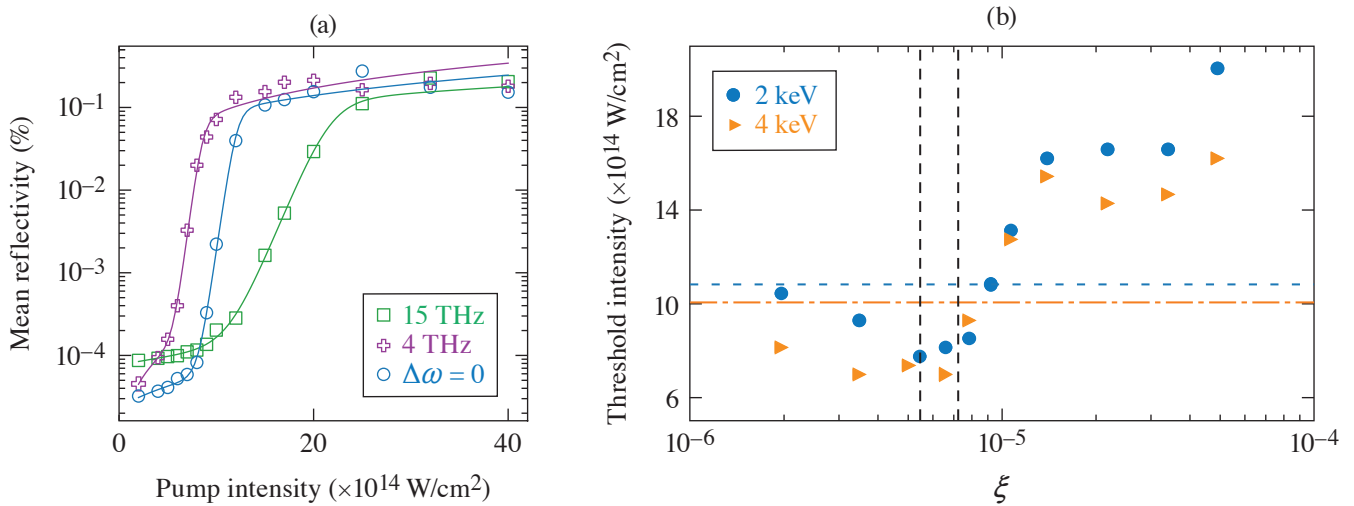


Figure 1
The maximum convective SRS gains in the fluid regime (open symbols) and kinetic regime (solid symbols) as functions of the normalized maximum chirp ξ . Four sets of simulations with bandwidth $\Delta\omega = 0$ (stars), 2 THz (circles), 6 THz (triangles), and 12 THz (squares) were performed in both the fluid and kinetic regimes. The vertical dashed line was obtained by evaluating Eq. (1).

TC15499JR

Figure 2(a) shows the time-averaged reflectivity as a function of pump intensity for three different bandwidths ($\Delta\omega = 0, 4$ and 15 THz). The sharp rise of the SRS reflectivity is a characteristic feature of kinetic inflation. The iSRS thresholds were obtained by fitting the reflectivity curve and then solving for the intensity corresponding to the steepest slope of the fitted function. The fitting function was $f(I) = \tanh[g(I - I_p) + a] (pI + q)$ for the free parameters $g, I_p, a, p,$ and q . The iSRS threshold is defined as the pump intensity corresponding to the inflection point of the fitted curve.

Figure 2(b) shows that the iSRS threshold as a function of the normalized maximum chirp ξ reaches its minimum when the maximum-gain condition is satisfied somewhere in the simulation region (between the vertical black dashed lines) regardless of the electron temperature. The horizontal dashed blue (dashed-dotted orange) line corresponds to the iSRS threshold at zero bandwidth for the 2-keV (4-keV) simulations. The iSRS threshold initially decreases as the maximum convective SRS gain is enhanced ($\Delta\omega\omega_m \leq \omega_p c/8L_n$) and then increases when the maximum local chirp rate of the pump exceeds the spatial detuning due to the density gradient ($\Delta\omega\omega_m \gg \omega_p c/8L_n$). The thresholds for the two temperatures are quantitatively close to each other



TC15501JR

Figure 2
(a) The fractional reflectivity as a function of the laser pump intensity for laser bandwidth, overlaid with the fits of the reflectivity data. (b) The iSRS threshold in terms of pump intensity as a function of the normalized maximum chirp ξ for two sets of simulations with different electron temperatures. The dotted blue (dashed-dotted orange) line corresponds to the iSRS threshold at zero bandwidth for 2-keV (4-keV) electron temperature. The two dashed vertical lines correspond to the maximum-gain condition at the minimum and maximum plasma densities.

for all ξ values. The fact that the iSRS threshold depends only weakly on the laser bandwidth alone is encouraging for ICF target design: for a given finite bandwidth, one can mitigate iSRS by tuning the maximum chirp away from the maximum-gain condition.

This material is based upon work supported by the Department of Energy National Nuclear Security Administration under Award Number DE-NA0003856, the University of Rochester, and the New York State Energy Research and Development Authority.

1. M. N. Rosenbluth, Phys. Rev. Lett. **29**, 565 (1972).

Measurements of Non-Maxwellian Electron Distribution Functions and Their Effect on Laser Heating

A. L. Milder,^{1,2} J. Katz,¹ R. Boni,¹ J. P. Palastro,¹ M. Sherlock,³ W. Rozmus,⁴ and D. H. Froula^{1,2}

¹Laboratory for Laser Energetics, University of Rochester

²Department of Physics and Astronomy, University of Rochester

³Lawrence Livermore National Laboratory

⁴Department of Physics, University of Alberta

Statistical mechanics governs the fundamental properties of many-body systems, and the corresponding velocity distributions dictate most material properties. In plasmas, a description through statistical mechanics is challenged by the fact that the movement of one electron affects many others through their Coulomb interactions, leading to collective motion. Although most of the research in plasma physics assumes equilibrium electron distribution functions, or small departures from a Maxwell–Boltzmann (Maxwellian) distribution, this is not a valid assumption in many situations. Deviations from a Maxwellian can have significant ramifications on the interpretation of diagnostic signatures and, more importantly, in our ability to understand the basic nature of plasmas. Uncertainties in the distribution function have implications across many areas of plasma physics including magnetic and inertial confinement fusion, astrophysics, and space sciences. The uncertainty in modeling of high-velocity electrons, including their nonlocal behavior, combined with the lack of experimental constraints has led to fundamental questions about the shape of electron velocity distributions.

In this summary, we present the first measurements of complete electron distributions without any assumptions on their shape or the underlying physics that produced them. A corresponding reduction in laser absorption, compared to classical absorption, of up to 37% was measured when the electron distributions were determined to be super-Gaussian. At these conditions the inverse bremsstrahlung heating dominated over thermalization by electron–electron collisions, and the measured absorption was in reasonable agreement with analytic predictions¹ that are commonly used in hydrodynamic modeling. To enable single-shot temporally and spatially resolved measurements of the electron distribution function over several orders of magnitude, an optical diagnostic was invented that uses the angular dependence of scattering to simultaneously access the noncollective and collective nature of plasmas. This first-principles measurement showed that during significant heating by the laser beams, the distributions had a super-Gaussian shape in the bulk ($v < 3 v_{th}$) with a Maxwellian tail ($v > 3 v_{th}$). The super-Gaussian bulk is associated directly with the inverse bremsstrahlung heating and is well reproduced by the previous computational work.² The departure from super-Gaussian at high velocities was predicted by Fourkal *et al.*,³ but these measurements show this deviation at a higher velocity. Particle simulations show improved agreement and demonstrate the importance of isotropic heating in accurately predicting the high-velocity tail.

Figure 1 shows the electron distribution function that was measured while five ultraviolet laser beams, with an overlapped intensity of $I_{UV}^{total} = 2.8 \times 10^{15} \text{ W/cm}^2$, uniformly heated an $\sim 1\text{-mm}^3$ volume of gas through inverse bremsstrahlung absorption. As predicted by theory,¹ the measurements show that slow electrons are preferentially heated to form a super-Gaussian electron distribution [Fig. 1(b)]. The measured electron distribution functions are well reproduced in the bulk by the heuristic scaling determined from early Fokker–Plank simulations,² where the electron distribution functions were parameterized by

$$f_m(v) = C_m \exp\left[-\left(\frac{v}{a_m v_{th}}\right)^m\right] \quad (1)$$

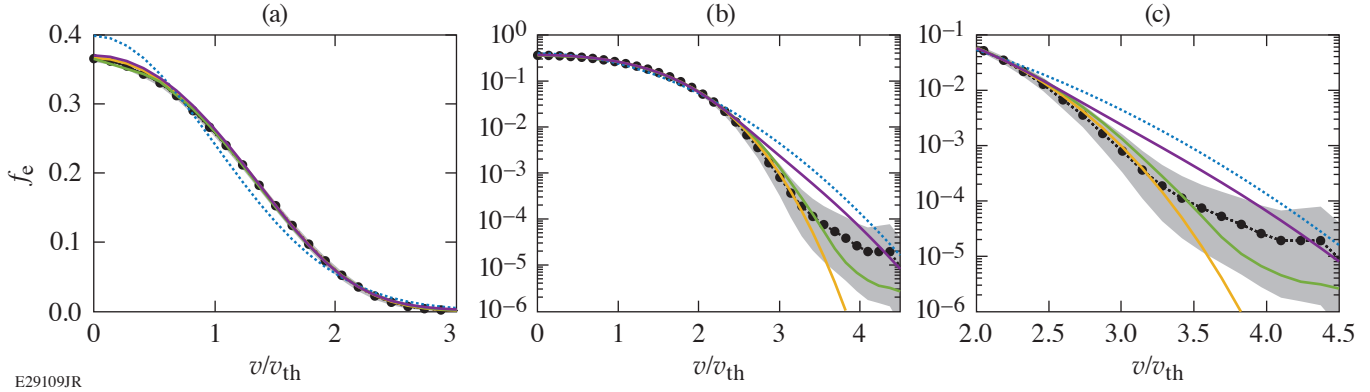


Figure 1

Electron distributions on (a) linear and logarithmic scales where (b) shows the complete velocity range, while (c) reduces the range to highlight the differences in the tails of the electron distribution functions. While the laser beams are heating the krypton plasma, the measured distribution (black points) is well reproduced in the bulk by a super-Gaussian function (orange curve) consistent with Matte *et al.*² [Eq. (2), $m = 3.9$]. A formalism describing the Maxwellian tail from Fourkal *et al.*³ (purple curve), a Maxwellian distribution (blue curve), and results from particle simulation (green curve) are shown. The 90% confidence interval on the measured distribution function (gray region) is shown.

with super-Gaussian order

$$m(\alpha) = 2 + \frac{3}{1 + 1.66/\alpha^{0.724}}, \quad (2)$$

where $\alpha = Zv_{\text{osc}}^2/v_{\text{th}}^2$ is the ratio of the inverse bremsstrahlung heating rate to the electron–electron collision rate and Z is the ionization state. Normalization constants (C_m , a_m) maintain the standard definitions of the first three moments of the distribution function. For the results shown in Fig. 1, the calculated electron distribution function [Eq. (1)] is in excellent agreement with the measurements for velocities less than $\sim 3v_{\text{th}}$ when using the overlapped intensity and the measured plasma conditions. The plasma conditions ($T_e = 1.16$ keV, $Z = 25$) were obtained from the simultaneous measurement of the angularly resolved electron plasma wave features and collective ion-acoustic wave features.

Figure 1(c) shows that the measured electron distribution transitions from a super-Gaussian to a Maxwellian shape at $\sim 3v_{\text{th}}$, whereas the theory from Fourkal *et al.*³ predicts an earlier transition around $\sim 2.5v_{\text{th}}$ and more electrons in the tail. This departure of Fourkal from a super-Gaussian distribution was calculated considering a single plane-wave electromagnetic source, where electrons oscillating in the laser field collide with electrons in the tail, modifying the distribution function at high energies. By introducing five overlapped beams, consistent with the experimental configuration, particle simulations using the code *Quartz* show that the number of electrons in the tail exceeds the super-Gaussian for velocities in the range $3.5v_{\text{th}} < v < 4.5v_{\text{th}}$, qualitatively consistent with the enhancement above super-Gaussian observed in the data. These results suggest that the increased uniformity due to multiple overlapped beams reduced the energy transferred to the high-velocity electrons.

Figure 2 shows that the measured laser absorption was significantly less than the absorption calculated assuming a plasma with a Maxwellian electron distribution. The absorption rapidly drops to $\sim 60\%$ of the Maxwellian expectation as the relative heating rate increases (large $Zv_{\text{osc}}^2/v_{\text{th}}^2$). When the inverse bremsstrahlung heating rate dominates over the electron–electron collision rate, the reduction in absorption is in reasonable agreement with the original predictions.¹

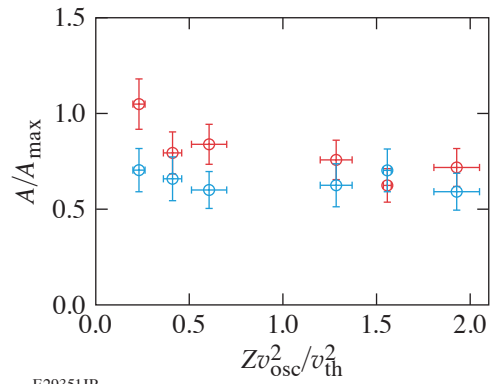


Figure 2

The measured (red circles) and calculated (blue circles) absorption, normalized to the absorption calculated assuming a Maxwellian electron distribution function, is plotted as a function of the ratio of the inverse bremsstrahlung heating rate to the electron–electron collision rate determined from the measured plasma conditions at the center of the plasma. Error bars represent one standard deviation propagated from uncertainties in the measured plasma conditions.

This material is based upon work supported by the Department of Energy National Nuclear Security Administration under Award Number DE-NA0003856, the University of Rochester, and the New York State Energy Research and Development Authority.

1. A. B. Langdon, Phys. Rev. Lett. **44**, 575 (1980).
2. J. P. Matte *et al.*, Plasma Phys. Control. Fusion **30**, 1665 (1988).
3. E. Fourkal *et al.*, Phys. Plasmas **8**, 550 (2001).

Nonlinear Spatiotemporal Control of Laser Intensity

T. T. Simpson,^{1,2} D. Ramsey,^{1,2} P. Franke,^{1,2} N. Vafaei-Najafabadi,³ D. Turnbull,¹ D. H. Froula,^{1,2} and J. P. Palastro¹

¹Laboratory for Laser Energetics, University of Rochester

²Department of Physics and Astronomy, University of Rochester

³Department of Physics and Astronomy, Stony Brook University

Spatiotemporal control over the intensity of a laser pulse has the potential to enable or revolutionize a wide range of laser-based applications that currently suffer from the poor flexibility offered by conventional optics. Specifically, these optics limit the region of high intensity to the Rayleigh range and provide little to no control over the trajectory of the peak intensity. In this summary, we introduce a nonlinear technique for spatiotemporal control—the “self-flying focus”—that produces an arbitrary trajectory intensity peak that can be sustained for distances comparable to the focal length.¹ The technique combines temporal pulse shaping and the inherent nonlinearity of a medium to customize the time and location at which each temporal slice within the pulse comes to its focus. As an example of its utility, simulations show that the self-flying focus can form a highly uniform, meter-scale plasma suitable for advanced plasma-based accelerators.

A wide range of laser-based applications share two requirements: (1) that the driving laser pulse maintain a high intensity over an extended distance, and (2) that the velocity of the peak intensity conform to some underlying process. Examples from across the fields of optics and plasma physics (such as THz and high-harmonic generation, photon acceleration, laser-wakefield and vacuum electron acceleration, Raman amplification, and plasma channel or filament formation) illustrate the ubiquity of these requirements. By providing unprecedented control over the trajectory of an intensity peak and the distance over which it can be sustained, spatiotemporal pulse shaping promises to expand the design space for these applications.^{2,3}

Existing methods utilize linear optical elements in the near field to structure a pulse with advantageous space–time correlations, but nonlinear processes, such as self-focusing, can also give rise to these correlations. Self-focusing occurs when the nonlinear optical response of a medium, quantified by the nonlinear refractive index reduces the phase velocity in regions of high intensity. The ratio of the instantaneous pulse power P to the critical power P_c parameterizes the effect. For temporal slices within a pulse with $P > P_c$, self-focusing overcomes diffraction. These slices undergo transverse collapse until their intensity reaches a threshold for activating a mechanism that can arrest the collapse. Because the distance over which a slice collapses depends on its value of P/P_c , the temporal profile of the power correlates time within the pulse to a collapse location [Fig. 1(a)].

The self-flying focus technique combines temporal pulse shaping with the inherent nonlinearity of a medium to control the velocity of an intensity peak over distances comparable to the focal length. Specifically, the instantaneous power determines the collapse location for each temporal slice, with the minimum and maximum powers setting the collapse range, while the pulse shape determines the time at which the intensity peak moves through these locations. A self-focusing arrest mechanism with an intensity threshold, such as ionization refraction, ensures that the maximum intensity of the peak remains nearly constant throughout the collapse range.

Figure 1 illustrates that the trajectory of self-focusing collapse can be controlled with temporal pulse shaping. A Gaussian pulse with $P > P_c$ focused into a nonlinear medium by an ideal lens exhibits a U-shaped collapse trajectory over the collapse

range (L_c) [Fig. 1(a)]. The lower-power temporal slices collapse closer to the linear focal point (f), while the higher-power slices collapse closer to the lens ($z = 0$). By shaping the pulse, the collapse point can move at a constant velocity through the collapse region [Fig. 1(b)]. In this example, the power decreases with time, ensuring that the higher-power temporal slices collapse earlier and closer to the lens, while the lower-power slices collapse later and farther from the lens. In both cases, the collapse velocity is decoupled from the group velocity of the pulse. Notably, because each temporal slice collapses to a different location, the duration of the resulting intensity peak can be substantially less than the overall pulse duration.

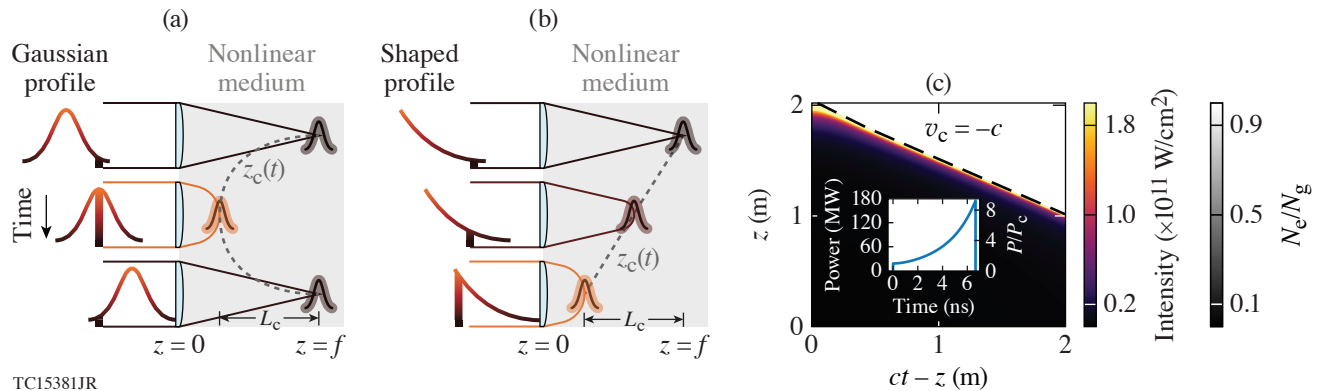


Figure 1

(a) Focusing a laser pulse with a Gaussian temporal profile with $P > P_c$ into a nonlinear medium creates a collapse point that traces out a U-shaped trajectory $z_c(t)$ over a distance L_c at a velocity v_c that is decoupled from the group velocity. (b) Focusing a temporally shaped pulse with $P > P_c$ can create a collapse point and intensity peak that follows any arbitrary trajectory—in this case, a constant, positive velocity—over a distance L_c . (c) On-axis intensity and electron density profiles from simulations of an $L_c = 1$ m self-flying focus pulse with $v_c = -c$ propagating through a lithium gas of density $N = 10^{19}/\text{cm}^3$ are shown. The incident power profile is plotted in the inset, with 20-ps exponential rise and fall times added to better represent a realistic shaped pulse. The intensity peak resulting from the collapse moves exactly at the desired trajectory and creates a smooth ionization front along that trajectory.

The ability to control the intensity trajectory over long distances makes the self-flying focus ideal for creating long plasma channels—a critical component in a number of applications, such as advanced laser-based accelerators and directed energy. Current techniques for creating long plasmas rely on filamentation through a dynamic balancing of self-focusing and plasma refraction, axicon focusing, variable wave front distortion, or the use of short wavelengths. Axicon focusing, for example, can suffer from significant pump depletion and ionization refraction by the end of the medium due to the forward propagation of the intensity peak. The self-flying focus has elements in common with filamentation but offers velocity control and does not necessarily require a short-pulse laser. Further, the ability to counter-propagate the intensity peak with respect to the pulse avoids ionization refraction, allowing for a wider range of focal geometries.

Here the self-flying focus is applied to the formation of a plasma channel necessary for the recently described “dephasingless” laser-wakefield accelerator.³ Figure 1(c) displays simulation results of a self-flying focus pulse with $v_c = -c$ propagating through lithium gas and triggering a sharp ionization front that travels at the same velocity (i.e., $v_f = -c$) over a meter. The negative collapse velocity allows the intensity peak to propagate through the background gas rather than the ionized plasma, thereby mitigating ionization refraction. The specific velocity of $-c$ was chosen such that an injected, relativistic electron bunch would be velocity matched to the plasma creation and therefore experience constant plasma conditions throughout its acceleration.

The self-flying focus can accommodate a wide range of parameters facilitating their use on various laser systems and in diverse applications. Notably, the self-flying focus could take advantage of long-pulse, high-energy laser systems, such as the National Ignition Facility or the OMEGA laser, to create intensity peaks with durations comparable to short-pulse lasers. Further, the self-flying focus could improve the formation of long, uniform plasma channels in other media for filamentation and directed energy-based applications.

This material is based upon work supported by the Department of Energy National Nuclear Security Administration under Award Number DE-NA0003856, the University of Rochester, and the New York State Energy Research and Development Authority.

1. T. T. Simpson *et al.*, *Opt. Express* **28**, 38,516 (2020).
2. D. H. Froula *et al.*, *Nat. Photonics* **12**, 262 (2018).
3. J. P. Palastro *et al.*, *Phys. Rev. Lett.* **124**, 134802 (2020).

Laser-Plasma Acceleration Beyond Wave Breaking

J. P. Palastro,¹ B. Malaca,² J. Vieira,² D. Ramsey,¹ T. T. Simpson,¹ P. Franke,¹ J. L. Shaw,¹ and D. H. Froula¹

¹Laboratory for Laser Energetics, University of Rochester

²Instituto de Plasmas e Fusão Nuclear, Instituto Superior Técnico, Universidade de Lisboa

Laser wakefield accelerators rely on the extremely high electric fields of nonlinear plasma waves to trap and accelerate electrons to relativistic energies over short distances. When driven strongly enough, plasma waves break, trapping a large population of the background electrons that support their motion. This limits the maximum electric field. We have discovered a novel regime of plasma wave excitation and wakefield acceleration that removes this limit, allowing for arbitrarily high electric fields. The regime, enabled by spatiotemporal shaping of laser pulses, exploits the property that nonlinear plasma waves with superluminal phase velocities cannot trap charged particles and are therefore immune to wave breaking. A laser wakefield accelerator operating in this regime provides energy tunability independent of the plasma density and can accommodate the large laser amplitudes delivered by modern and planned high-power, short-pulse laser systems.

Armed with a vision of smaller-scale, less-expensive accelerators and empowered by advances in laser technology, the field of “advanced accelerators” has achieved rapid breakthroughs in both electron and ion acceleration.¹ In laser wakefield acceleration (LWFA), in particular, a high-intensity laser pulse drives a plasma wave that can trap and accelerate electrons with a field nearly 1000× larger than the damage-limited field of a conventional radio-frequency accelerator.² Progress in the field of LWFA exploded with the advent of high-power, broadband amplifiers, which delivered ultrashort pulses with durations less than the plasma period. While advances in laser technology continue to deliver ever-shorter and more-powerful pulses, the current path to higher electron energies calls for longer pulses to match the plasma period at lower densities.

The substantial bandwidth provided by modern laser systems offers an alternative approach to designing LWFA’s and increasing the maximum electron energy—spatiotemporal pulse shaping.^{3,4} Spatiotemporal pulse shaping provides the flexibility to structure the pulse with advantageous space–time correlations that can be tailored to an application. As an example, stretching the region over which a laser pulse focuses and adjusting the relative timing at which those foci occur provides control over the velocity of an intensity peak independent of the group velocity.⁵ In LWFA, because the phase velocity of the plasma wave (v_p) equals the velocity of the ponderomotive potential, a typical pulse, with an intensity peak that travels at the group velocity (v_g), will drive a subluminal wake ($v_p = v_g < c$). The intensity peak of a shaped pulse, on the other hand, can travel at or faster than the vacuum speed of light, such that $v_p \geq c$ (Ref. 5).

The phase velocity of a subluminal plasma wave determines the maximum electric field that the plasma wave can support. A laser pulse propagating in a plasma with a peak normalized vector potential $a_0 = eA_0/m_e c$ expels electrons from its path and leaves behind a region of net positive charge. The resulting electrostatic field accelerates the expelled electrons back into this region in an attempt to neutralize that charge. When driven by a pulse with a sufficiently large peak amplitude ($a_0 = a_{wb}$), the electrostatic field will accelerate the electrons up to the phase velocity of the wave. At this point, the wave breaks, trapping a significant fraction of the electrons that supported its motion. For a 1-D, cold plasma wave, the wave-breaking field depends only on the phase velocity, $E_{wb} = [2(\gamma_p - 1)]^{1/2}$, where $\gamma_p = (1 - \beta_p^2)^{-1/2}$, $\beta_p = v_p/c$, the field has been normalized by $em_e c/\omega_p$,

$\omega_p = (en_0/m_e \epsilon_0)^{1/2}$ is the plasma frequency, and n_0 is the ambient electron density. The unwanted injection and trapping of charge, or dark current, resulting from wave breaking reduces the accelerating field and increases the energy spread of the accelerated electron bunch.

The intensity peak of a spatiotemporally shaped pulse can drive a plasma wave with a superluminal phase velocity ($\beta_p > 1$), precluding wave breaking altogether: the electrostatic field of the plasma wave can never accelerate electrons up to its phase velocity ($\beta_e < \beta_p$). This property enables a novel regime of LWFA that (1) can have arbitrarily high accelerating fields and (2) avoids unwanted, continuous injection and trapping of electrons. The idea is to accelerate electrons with a large, unbounded electric field over half a dephasing length—the distance over which a highly relativistic electron experiences one-half period of the wake.

Figure 1 illustrates the design space for superluminal LWFA. When $\beta_p \geq 1$, wave breaking does not occur, and both the phase velocity (i.e., the driver velocity) and the vector potential can be used to tune the energy gain independent of the plasma density. This density-independent tunability of superluminal LWFA allows for operation at higher plasma densities with shorter matched pulses. As a result, this new regime can (1) take advantage of the high-intensity, ultrashort pulses delivered by modern and planned high-power laser systems and (2) avoid the experimental complication of having to create long, low-density plasmas to increase the energy gain.

In contrast to subluminal wakes, the energy gain for a superluminal wake ($\beta_p \geq 1$) increases indefinitely with a_0 . A subluminal plasma wave driven with an $a_0 > a_{wb}$ will break, trapping a significant fraction of the background electrons. The electrostatic field of the trapped electrons cancels that of the wakefield and diminishes the energy gain. Figure 2 shows the results of 1-D *OSIRIS* particle-in-cell simulations⁶ that demonstrate this for $a_0 = 15$ after ~ 0.7 of a dephasing length. For nearly the same value of $|\gamma_p^2|$, the superluminal wake [Fig. 2(a)] has maintained its accelerating field, while injection and trapping have significantly reduced the field of the subluminal wake [Fig. 2(b)].

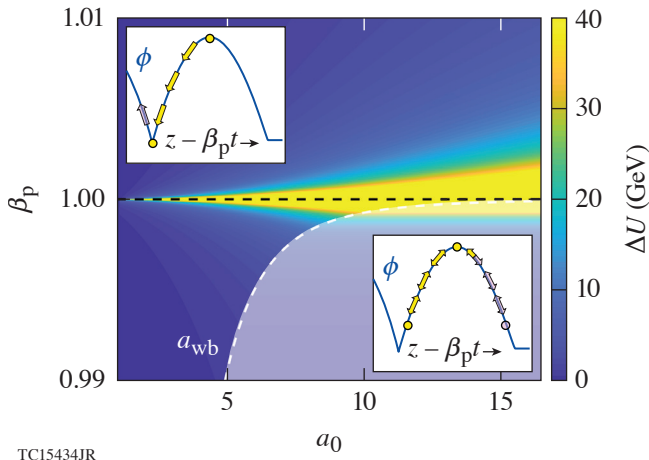


Figure 1
 Design space for superluminal ($\beta_p \geq 1$) and subluminal ($\beta_p < 1$) LWFA. Wave breaking limits the design space for subluminal LWFA when the amplitude of the driving laser pulse exceeds a threshold value ($a_0 > a_{wb}$). A superluminal LWFA can take advantage of arbitrarily high intensity, preserving the structure of the wakefield and its peak accelerating field. The top and bottom insets illustrate the differences in the dynamics of an electron that achieves the maximum energy gain injected at rest into the potential of a super and subluminal wake, respectively. The solid (yellow) arrows mark the path over which the electron gains energy.

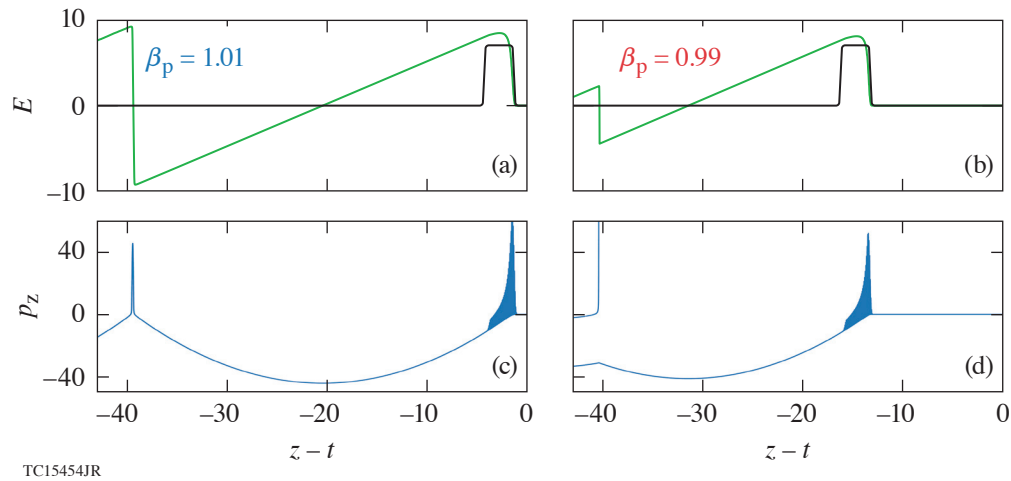


Figure 2

A comparison of the electric field of the wake and electron phase space for [(a),(c)] a superluminal and [(b),(d)] a subluminal wake with $\beta_p = 1.01$ and $\beta_p = 0.99$, respectively. The phase velocities were chosen to make the distinction between the two cases clear throughout the summary. The driver intensity, shown in black for reference, has $a_0 = 15$ and a square pulse shape with duration $\tau = \pi$. The superluminal wake maintains its structure and maximum electric field. Wave breaking of the subluminal wake leads to the injection and trapping of a large population of electrons, which load the wake and diminish its maximum field.

The work published here was supported by the U.S. Department of Energy Office of Fusion Energy Sciences under contract Nos. DE-SC0016253 and DE-SC0021057, the Department of Energy under cooperative agreement no. DE-NA0003856, the University of Rochester, and the New York State Energy Research and Development Authority.

1. C. Joshi, S. Corde, and W. B. Mori, *Phys. Plasmas* **27**, 070602 (2020).
2. E. Esarey, C. B. Schroeder, and W. P. Leemans, *Rev. Mod. Phys.* **81**, 1229 (2009).
3. A. Sainte-Marie, O. Gobert, and F. Quéré, *Optica* **4**, 1298 (2017).
4. D. H. Froula *et al.*, *Nat. Photonics* **12**, 262 (2018).
5. J. P. Palastro *et al.*, *Phys. Rev. Lett.* **124**, 134802 (2020).
6. R. A. Fonseca *et al.*, in *Computational Science – ICCS 2002*, edited by P. M. A. Sloot *et al.*, Lecture Notes in Computer Science, Vol. 2331 (Springer, Berlin, 2002), pp. 342–351.

Wide-Ranging Equations of State for B_4C Constrained by Theoretical Calculations and Shock Experiments

S. Zhang,^{1,2} M. C. Marshall,^{1,2} L. H. Yang,² P. A. Sterne,² B. Militzer,³ M. Däne,² J. A. Gaffney,² A. Shamp,² T. Ogitsu,² K. Caspersen,² A. E. Lazicki,² D. Erskine,² R. A. London,² P. M. Celliers,² J. Nilsen,² and H. D. Whitley²

¹Laboratory for Laser Energetics, University of Rochester

²Lawrence Livermore National Laboratory

³Departments of Earth and Planetary Science and Astronomy, University of California, Berkeley

The design of high-energy-density (HED) and inertial confinement fusion (ICF) experiments requires a good description of the ablator equation of state (EOS). Currently, CH plastics are typically used as ablators, and their EOS has been extensively studied (see Fig. 1). However, the formation of condensed phase microstructures, species separation, and mixing with the DT fuel during an implosion could affect the performance of the ICF target or interpretation of HED experiments.^{1–3} Other materials with higher densities and hardness, such as boron, have been explored as alternative ablators. In the past three years, we have combined various theoretical approaches with planar shock experiments and benchmarked the EOS of boron (B)⁴ and boron nitride (BN)⁵ over wide ranges of density–temperature conditions. Under constraints provided by these data, new *Purgatorio*-based EOS models (LEOS 50 for B and X52 for BN) have been constructed and made available for use in hydrodynamic simulations. As a follow-up, this work presents a comprehensive study of the EOS of boron carbide (B_4C), another important member in the family of boron materials.

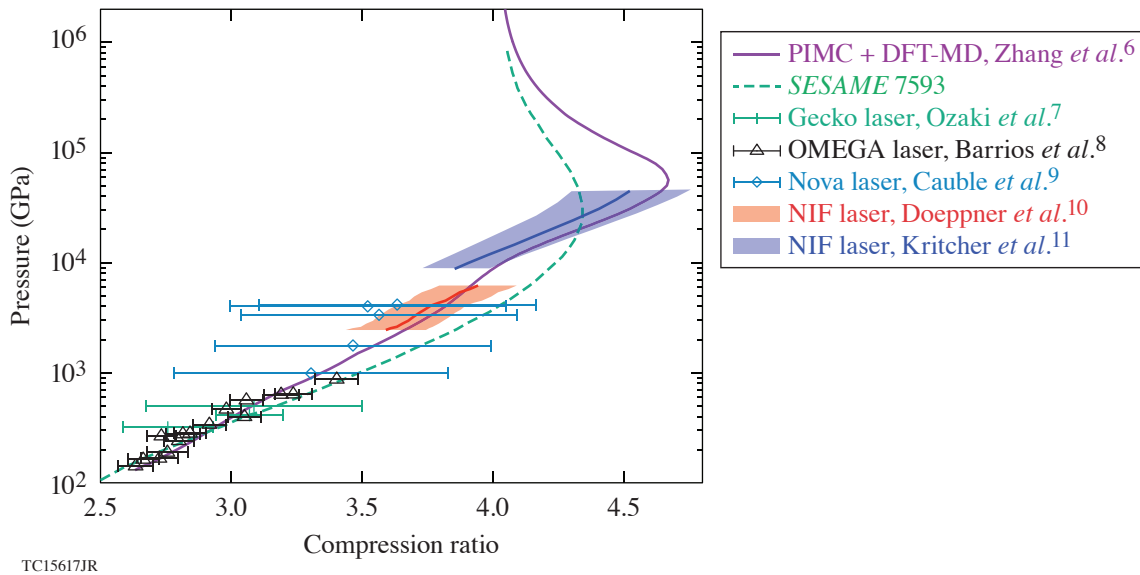


Figure 1

The Hugoniot of CH polystyrene from first-principles computations is consistent with planar shock experiments and verified by the latest spherically converging shock data at the National Ignition Facility (NIF). In comparison, the Thomas–Fermi-based *SESAME* 7593 model predicts the Hugoniot to be much smoother around the compression maximum and is invalidated by the NIF data. The initial sample density $\rho_0 = 1.05 \text{ g/cm}^3$.

The computational methods that we have employed include path-integral Monte Carlo (PIMC) and density functional theory molecular dynamics (DFT-MD), which provide a wide-ranging, internally coherent first-principles EOS for B_4C in hot plasma, warm dense matter, and condensed liquid states. The calculations are jointly benchmarked by computations using an all-electron Green's function Korrington–Kohn–Rostoker (MECCA) and an activity expansion (ACTEX) approach. The theoretical predictions of the Hugoniot EOS are cross validated by comparisons with Hugoniot measurements up to 6100 GPa from planar shock experiments performed on the NIF.

Figure 2 summarizes the major findings of this research, including EOS comparisons between PIMC and DFT-MD, as well as Hugoniot comparisons between predictions by various computational methods or semi-empirical models and shock experiments. Note that our DFT-MD calculations have been performed in multiple ways, including one that uses projector augmented wave (PAW) potentials with plane-wave basis (PAWpw) and another one that uses optimized norm-conserving Vanderbilt (ONCV) potentials combined with pw basis or a Fermi-operator expansion. The PAW potentials have a frozen $1s$ core, which limits the PAWpw computations to temperatures below 5×10^5 K and moderately high densities (we considered up to 20.07 g/cm^3). We used all-electron ONCV potentials for calculations at temperatures up to 1.35×10^6 K and densities up to 50.18 g/cm^3 . The EOS produced by the ONCV calculations matches both the PAWpw data at low temperatures and the PIMC data at high temperatures very well, as shown with overlapping isotherms in Fig. 2(a).

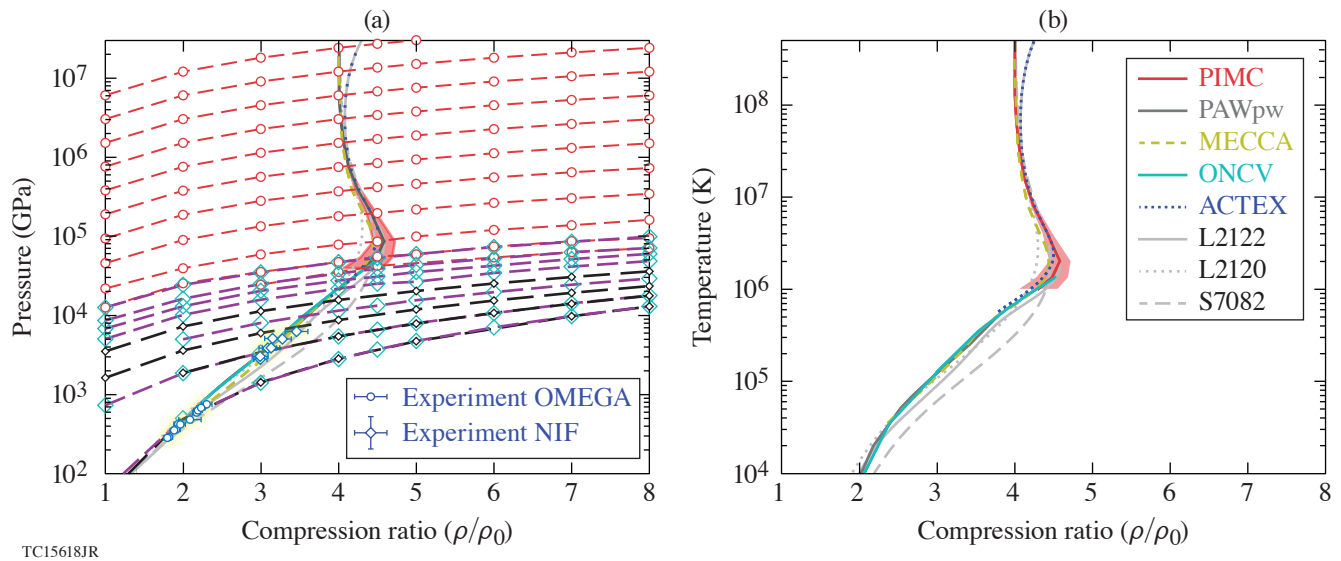


Figure 2

The (a) pressure–compression and (b) temperature–compression Hugoniot of B_4C from various computational methods (PIMC, PAWpw, ONCV, MECCA, and ACTEX) in comparison with predictions by different EOS models (L2122/2120: LEOS models; S7082: a *SESAME* model) and measurements by two separate laser shock experiments (OMEGA, by Fratanduono *et al.*,⁶ and the NIF, this work). The initial sample density $\rho_0 = 2.51 \text{ g/cm}^3$. The shaded area around the lower end of the PIMC Hugoniot curve represent 1σ uncertainty in the corresponding Hugoniot density due to EOS errors. In (a), EOS data along selective isotherms from three approaches are also shown with dashed lines and points (PIMC in red circles, ONCV in cyan diamonds, and PAWpw in small black diamonds). The lowest two isotherms for ONCV (and PAWpw) correspond to temperatures of 10^4 and 1.26×10^5 K, respectively. The highest two isotherms for ONCV (and the lowest two by PIMC) correspond to 1.01×10^6 and 1.35×10^6 K, respectively. The deviation between PIMC/L2120 (and MECCA) and ACTEX/L2122 Hugoniot curves above 106 GPa and 2×10^7 K is due to the electron relativistic effect, which is considered in ACTEX and L2122 but not in PIMC/L2120 (and not fully in MECCA).

Our calculated Hugoniot curves using the different theoretical approaches show good consistency with each other and overall agreement with two independent sets of experimental measurements at 200 to 6100 GPa. At the highest pressure of the OMEGA data¹² and the lowest pressure of the NIF data, our DFT-MD predictions of the Hugoniot are slightly stiffer than the experiment,

which could be worthwhile to study in the future. Assisted by the theoretical predictions, we estimate the corresponding Hugoniot temperatures for the NIF data to be in the range of 1 to 5×10^5 K. Our Hugoniot results also show overall good consistency with the L2122 model and predict B₄C to have a maximum compression ratio of 4.55 at 9×10^4 GPa and 2×10^6 K, below which L2122 predicts B₄C to be slightly softer. In comparison, Thomas–Fermi model L2120 predicts B₄C at the compression maximum to be stiffer by $\sim 6\%$ and *SESAME* 7082 predicts B₄C to be much softer at pressures of 800 to 3×10^4 GPa.

We compared the EOS of B₄C between our first-principles predictions and L2122 and found a maximum pressure discrepancy of $\sim 18\%$ occurring at 6×10^3 to 2×10^5 K. We have therefore constructed three new EOS models (L2123 to 2125) by variations of the cold curve and the ion thermal EOS model to span the range of experimental error bars. We then performed a series of 1-D hydrodynamic simulations of direct-drive implosions with a B₄C ablator described by the four EOS models (L2122 to 2125) based on a polar-direct-drive exploding-pusher platform.^{13–15} The results showed that the performance is insensitive to the EOS variations.

This material is based upon work supported by the Department of Energy National Nuclear Security Administration under Award Number DE-NA0003856, the University of Rochester, and the New York State Energy Research and Development Authority. This work was in part performed under the auspices of the U.S. Department of Energy by Lawrence Livermore National Laboratory under Contract No. DE-AC52-07NA27344.

1. D. S. Clark *et al.*, *Phys. Plasmas* **23**, 056302 (2016).
2. S. Yu Gus'kov *et al.*, *J. Russ. Laser Res.* **38**, 173 (2017).
3. S. Zhang and S. X Hu, *Phys. Rev. Lett.* **125**, 105001 (2020).
4. S. Zhang *et al.*, *Phys. Rev. E* **98**, 023205 (2018).
5. S. Zhang *et al.*, *Phys. Rev. B* **99**, 165103 (2019).
6. S. Zhang *et al.*, *J. Chem. Phys.* **148**, 102318 (2018).
7. N. Ozaki *et al.*, *Phys. Plasmas* **16**, 062702 (2009).
8. M. A. Barrios *et al.*, *Phys. Plasmas* **17**, 056307 (2010).
9. R. Cauble *et al.*, *Phys. Plasmas* **4**, 1857 (1997); R. Cauble *et al.*, *Phys. Rev. Lett.* **80**, 1248 (1998).
10. T. Döppner *et al.*, *Phys. Rev. Lett.* **121**, 025001 (2018).
11. A. L. Kritcher *et al.*, *Nature* **584**, 51 (2020).
12. D. E. Fratanduono *et al.*, *Phys. Rev. B* **94**, 184107 (2016).
13. C. L. Ellison *et al.*, *Phys. Plasmas* **25**, 072710 (2018).
14. H. D. Whitley *et al.*, “Comparison of Ablators for the Polar Direct Drive Exploding Pusher Platform,” *Physics Archive*, <https://arxiv.org/abs/2006.15635> (2020).
15. C. B. Yeaman *et al.*, “High Yield Polar Direct Drive Fusion Neutron Sources at the National Ignition Facility,” submitted to *Nuclear Fusion*.

A Novel Photomultiplier Tube Neutron Time-of-Flight Detector

V. Yu. Glebov, C. Stoeckl, C. J. Forrest, J. P. Knauer, O. M. Mannion, M. H. Romanofsky, T. C. Sangster, and S. P. Regan

Laboratory for Laser Energetics, University of Rochester

A traditional neutron time-of-flight (nTOF) detector used in inertial confinement fusion¹ usually consists of a scintillator optically coupled to a photomultiplier tube (PMT). For accurate ion-temperature measurements in DT implosions, a scintillator- and PMT-based detector must use a fast scintillator and fast microchannel plate (MCP) PMT. Even with the fastest scintillators, the scintillator light decay significantly contributes to the instrument response function (IRF) of the nTOF detector. A novel PMT nTOF detector developed at LLE has a MCP photomultiplier tube in a housing without a scintillator. This PMT nTOF detector is less sensitive than a traditional nTOF detector with a scintillator and can be used only in high-yield (typically larger than 10^{13} DT) implosions. Eliminating the scintillator removes the scintillator decay from the IRF and makes the detector faster. The PMT nTOF is the fastest nTOF detector currently in use on OMEGA.

The PMT nTOF detector made of Photek²—a PMT110 gated photomultiplier with a 10-mm-diam photocathode and a single-stage MCP—was tested at 5.6 m from the target in the P2 open line of sight (LOS) on OMEGA. The nTOF signal was recorded on a 2.5-GHz, 10-GS/s Keysight DSOS254A oscilloscope. The measured neutron temporal trace signal was fit with a convolution of a Gaussian and an exponential decay function, as described in detail in Ref. 3. The fit was performed at up to 50% of the falling slope of the signal.

To determine if the measured neutron signal originates in the window or in the MCP, a comparison test was performed of the PMT nTOF with no gate and with a gate (see Fig. 1). The electronic gate energizes the PMT at select times to discriminate unwanted signals. During the shot with the gate, the Photek gate unit produces a 250-V pulse that prevents photoelectrons from the photocathode from reaching the MCP. If a neutron signal is produced by direct interaction of neutrons with the MCP, the gate will have no effect.

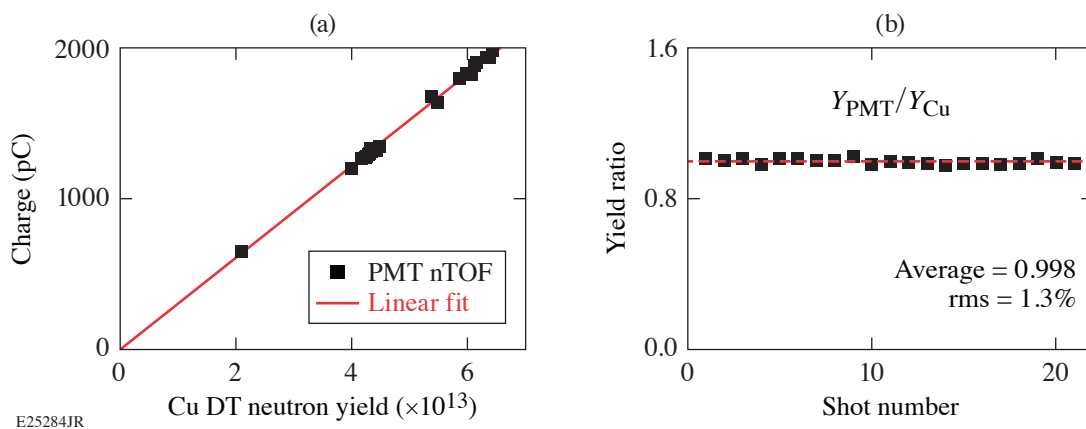


Figure 1

(a) The neutron signal in shot 91551 with a yield of 3.7×10^{13} recorded by a PMT nTOF with no gate; (b) the neutron signal in shot 91547 with a yield of 4.1×10^{13} recorded by a PMT nTOF with a gate.

However, in shot 91551 with a DT yield of 3.7×10^{13} and no gate pulse in the PMT, the neutron pulse charge was 223.10 pC, and in shot 91547 with a DT yield of 4.1×10^{13} and with a gate pulse in the PMT, the neutron pulse charge was 5.25 pC. One can calculate from the yields and charges of these two shots that only 2% of the neutron signal is produced by direct interaction with the MCP, and the remaining 98% of the neutron signal in the PMT nTOF is produced by photoelectrons from the photocathode. The photoelectrons are produced in the PMT fused-silica window in many complex nuclear processes⁴ ranging from (n,γ) interactions and following Compton scattering to “knock-on” O¹⁶ and Si²⁸ ions that produce low-energy electrons during slowdown.

The PMT nTOF detector based on Photek² PMT140 was permanently installed on the wall of the OMEGA Target Bay’s southeast corner in the P4F line of sight at 15.9 m from the target with 10-mm-thick lead shielding in front. At 15.9 m, the PMT140 is operated at -4.2 kV, corresponding to a PMT gain of 400. The PMT nTOF in this location is capable of measuring DT yields from 1×10^{12} to 3×10^{14} . The PMT nTOF at the 15.9-m location was yield calibrated against the copper activation diagnostic as shown in Fig. 2(a). The ratio of DT neutron yields measured by the PMT nTOF and the copper activation are shown in Fig. 2(b). The measured neutron yield shot-to-shot precision of the PMT nTOF at the 15.9-m location is better than 1.3%.

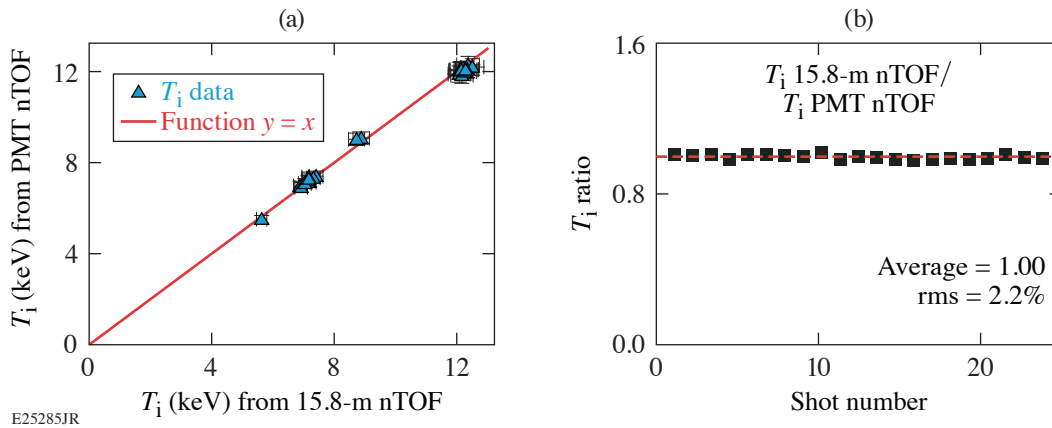


Figure 2

(a) DT neutron calibration of the 15.9-m PMT nTOF against copper activation; (b) the ratio of DT yield measured by the 15.9-m PMT nTOF and copper activation.

For ion-temperature calibration of the 15.9-m PMT nTOF, we used a traditional 15.8-m nTOF detector with a 40-mm-diam, 20-mm-thick BC422Q scintillator coupled to a PMT140 and located at 15.8 from target chamber center (TCC). Both detectors use the same type of PMT, the same scopes (located at a similar distance from the target), and the same 10-mm lead front shielding. The only difference between the two nTOF detectors is whether or not a scintillator is included. The fitting parameters of the PMT nTOF detector at the 15.9-m location were adjusted to match the ion-temperature measurements of the 15.8-m nTOF detector recorded in room-temperature, thin-shell targets with high-adiabat implosions in which the ion-temperature distribution is considered isotropic. Figure 3(a) shows the ion temperature measured by the PMT nTOF versus the ion temperature measured by the 15.8-m nTOF. The ratio of ion temperatures measured by these two similar independent detectors is shown in Fig. 3(b). The standard deviation for the ion temperature ratio is 2.2%, which corresponds to the standard deviation for a single detector of 1.56%. Therefore, the ion temperature measurement precision of the 15.9-m PMT nTOF is 1.6%.

Two additional fast nTOF detectors were constructed along opposing (antipodal) lines of sight to complete a suite of nTOF detectors on OMEGA for hot-spot flow-velocity measurements.⁵ The H4D and H17E lines of sights were selected for nTOF detector deployment. Since hot-spot flow-velocity measurements require⁵ timing uncertainties <100 ps, the fastest PMT nTOF based on 10-mm-diam MCP PMT’s were selected for these antipodal nTOF’s. Two 10-mm-diam Hamamatsu⁶ MCP PMT’s were available at LLE: one ungated R3809U-52 and one normally gated “OFF” R5916U-50. To record x-ray IRF from the Hamamatsu PMT during OMEGA timing-calibration shots, each detector has a 1-mm-thick aluminum front PMT housing and each OMEGA sub-port has a 5-mm aluminum window. The ungated R3809U-52 PMT was installed in the H4D LOS at 10.4 m from TCC, and the gated R5916U-50 PMT was installed at the H17E 4.9-m location. Both detectors were installed with their faces perpendicular to the LOS of the TCC.

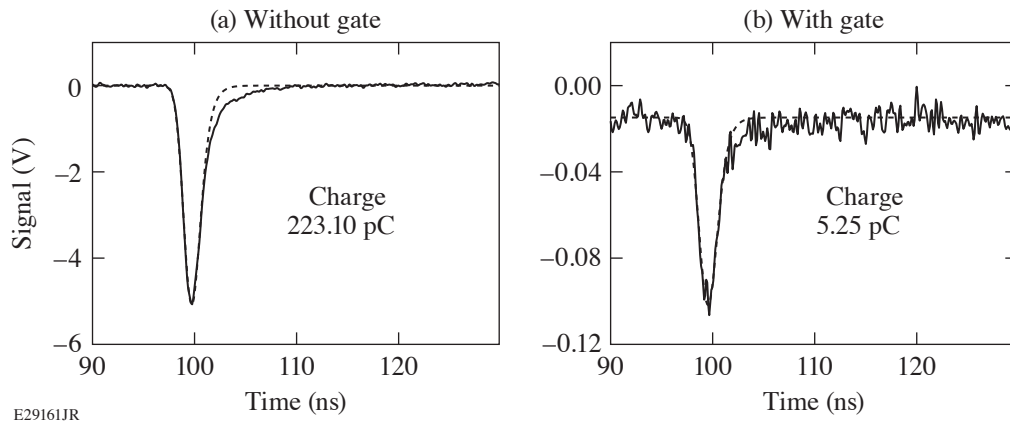


Figure 3

(a) Ion temperature from the 15.9-m PMT nTOF versus ion temperature from the 15.8-m nTOF; (b) the ratio of ion temperatures from the 15.8m nTOF and 15.9-m PMT nTOF detectors.

The neutron IRF is very important for accurate measurement of the neutron energy and hot-spot flow velocity⁵ in DT implosions. Since, in the absence of the short impulse of 14-MeV neutrons, it is impossible to measure neutron IRF directly, a two-step process described in detail in Ref. 7 was used. During the first step, an x-ray IRF was experimentally measured, and during the second step, the neutron IRF was constructed by correcting x-ray IRF for the DT neutron propagation time modeled in MCNP (Monte Carlo neutron particle code). The x-ray IRF's for the H4D and the H17E PMT nTOF detectors were measured with a 100-ps laser pulse on a gold target. Both detectors have a subnanosecond x-ray IRF: the H4D nTOF has 540 ± 20 ps FWHM and the H17E nTOF has 360 ± 12 ps FWHM. The uncertainty on the IRF FWHM is taken from the standard error of the mean FWHM from the set of IRF measurements. The 14-MeV neutrons' propagation time through a 3.2-mm-thick PMT window is very short (62 ps), and convolution of an x ray with MCNP simulation is practically the same as an x-ray IRF. Using the constructed neutron IRF, the hot-spot flow velocity in DT fusion experiments can be determined from the H4D and the H17E PMT nTOF signals using a forward-fitting method.⁷ The H4D and H17E forward fits for shot 95201 with a yield of 1.1×10^{14} and T_i of 4.3 keV are shown in Fig. 4. The PMT nTOF detector in the H17E location has a negligible background, and a good fit is achieved with only the IRF. The PMT nTOF detector in the H4D location has an additional gamma background from (n, γ) interactions with the Target Bay wall. For proper fitting of a neutron peak, a modified Gaussian background contribution is included in the forward fit and determined on each shot [see Fig 4(a)]. The operational yield range for the H4D and H17E PMT nTOF detectors is from 1×10^{13} to 2×10^{14} . The commissioning of the H4D and H17E PMT nTOF detectors completed the suite of nTOF detectors on OMEGA for hot-spot motion measurements.⁵

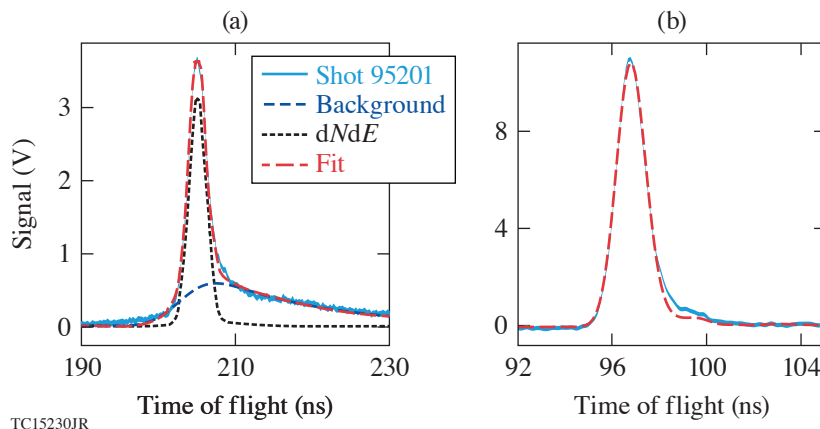


Figure 4

The forward fits of neutron signals from (a) H4D and (b) H17E nTOF detectors.

This material is based upon work supported by the Department of Energy National Nuclear Security Administration under Award Number DE-NA0003856, the University of Rochester, and the New York State Energy Research and Development Authority.

1. J. D. Lindl, *Inertial Confinement Fusion: The Quest for Ignition and Energy Gain Using Indirect Drive* (Springer-Verlag, New York, 1998).
2. Photek Ltd., St. Leonards on Sea, East Sussex, TN38 9NS, United Kingdom, <http://www.photek.com/>.
3. T. J. Murphy, R. E. Chrien, and K. A. Klare, *Rev. Sci. Instrum.* **68**, 610 (1997).
4. A. S. Moore *et al.*, *Rev. Sci. Instrum.* **89**, 10I120 (2018).
5. O. M. Mannion *et al.*, *Nucl. Instrum. Methods Phys. Res. A* **964**, 163774 (2020).
6. Hamamatsu Photonics K.K., Hamamatsu City, Shizuoka, Japan 4308587, <https://www.hamamatsu.com/us/en/index.html>.
7. R. Hatarik *et al.*, *J. Appl. Phys.* **118**, 184502 (2015).

A Generalized Forward Fit for Neutron Detectors with Energy-Dependent Response Functions

Z. L. Mohamed,^{1,2} O. M. Mannion,^{1,2} E. P. Hartouni,³ J. P. Knauer,¹ and C. J. Forrest¹

¹Laboratory for Laser Energetics, University of Rochester

²Department of Physics and Astronomy, University of Rochester

³Lawrence Livermore National Laboratory

To date, most analyses of neutron time-of-flight (nTOF) data from inertial confinement fusion experiments have focused on the relatively small range of energies corresponding to the primary neutrons from D–D and D–T fusion. These analyses have therefore employed instrument response functions (IRF's) corresponding to monoenergetic 2.45- or 14.03-MeV neutrons. For analysis of time-of-flight signals corresponding to broader ranges of neutron energies, accurate treatment of the data requires the use of an energy-dependent IRF. This work describes interpolation of the IRF for neutrons of arbitrary energy, construction of an energy-dependent IRF, and application of this IRF in a forward fit via matrix multiplication.

The measured nTOF signal includes effects from the detector's IRF such that the relationship between the neutron energy spectrum and the measured signal is not immediately obvious. One method of interpreting an nTOF signal is the forward-fit technique,¹ which involves the convolution of a model neutron energy spectrum with the detector IRF. In the absence of bright, pulsed monoenergetic neutron sources, the total neutron IRF cannot be directly measured. The total neutron IRF is instead constructed by convolving a measured x-ray response with an energy-dependent neutron interaction response. The measured x-ray response accounts for the detector's response to a short pulse of incident energy, while the energy-dependent neutron interaction response accounts for neutron transport through the detector and can be calculated using a particle transport code such as MCNP.²

The oscilloscope-recorded nTOF signal $m(t)$ can be understood as the superposition of the detector's response to a neutron of incident energy E , weighted by the number of neutrons incident on the detector at that energy. The variable t represents the time scale recorded on the oscilloscope, while t' represents the neutron's time of arrival at the detector. If the number of neutrons detected per unit energy is given by $dN/dE[E(t')]$, the detector's temporal response for a given incident neutron energy is given by $R[E(t'), t-t']$, the Jacobian describing the conversion from neutron energy to nTOF is dE/dt' , and the detector's calibration constant is C , then the measured signal can be written as a Fredholm integral of the first kind given by

$$m(t) = C \int_0^{t'} \frac{dN}{dE} [E(t')] \frac{dE}{dt'} [E(t')] R[E(t'), t-t'] dt'. \quad (1)$$

The equation for the forward fit with an energy-dependent IRF can also be written as a sum such that Eq. (1) becomes

$$m(t_k) = \sum_{i=0}^k P [E(t'_i)] R [E(t'_i), t_k - t'_i].$$

This sum can be represented by the matrix multiplication $\vec{m} = \mathbf{T}\vec{P}$, where \vec{P} is the vector of prediction of length N_p , \vec{m} is the vector of measured values of length $N_m = N_p + N_r - 1$, and \mathbf{T} is a Toeplitz matrix of the response vector³ with shape $N_m \times N_p$ given by

$$T = \begin{bmatrix} r_{0,0} & 0 & \dots & 0 & 0 \\ r_{0,1} & r_{1,0} & \dots & \dots & \dots \\ r_{0,2} & r_{1,1} & \dots & 0 & 0 \\ \dots & r_{1,2} & \dots & r_{N_{p-1},0} & 0 \\ r_{0,N_r-1} & \dots & \dots & r_{N_{p-1},1} & r_{N_p,0} \\ r_{0,N_r} & r_{1,N_r-1} & \dots & \dots & r_{N_p,1} \\ 0 & r_{1,N_r} & \dots & r_{N_{p-1},N_r-2} & \dots \\ 0 & 0 & \dots & r_{N_{p-1},N_r-1} & r_{N_p,N_r-2} \\ \dots & \dots & \dots & r_{N_{p-1},N_r} & r_{N_p,N_r-1} \\ 0 & 0 & 0 & \dots & r_{N_p,N_r} \end{bmatrix}. \quad (2)$$

Note that the first index of each matrix element corresponds to energy $E\{t'_j\}$, while the second index corresponds to time $t_k - t'_i$ (i.e., the index of a specific entry within the array of $R[E(t'_i), t_k - t'_i]$). Each column represents a monoenergetic IRF. It is clear that several monoenergetic IRF's must be generated in order to construct the Toeplitz matrix since each column of the matrix represents a response function of a different energy. This is best accomplished by generating a representative set of neutron interaction responses, convolving them with the measured x-ray IRF, and interpolating the total IRF.

Uncertainty in the IRF is introduced mainly by the uncertainty in the measured x-ray IRF. Minimization must be carried out in order to include both Poisson-distributed uncertainties from the number of neutrons detected as well as Gaussian-distributed uncertainties from digitization noise. Details of the error propagation that is necessary to construct the correct χ^2 fit metric are included in the full length paper.⁴

As an example of the application of this method, an analysis of synthetic data relevant to T-T fusion experiments at the Omega Laser Facility is discussed. This example is used to illustrate the differences between a forward fit that uses an energy-dependent IRF and a forward fit that uses a monoenergetic IRF. Use of the energy-dependent IRF results in an accurate inference of the fit parameters of interest. The inferred masses of the ⁵He ground state and first excited state are minimally affected since the mass is related to the mean neutron energy. Use of the monoenergetic 2.45-MeV (DD) IRF affects the inferred width and magnitude of the ground state significantly (>20% change). Use of the monoenergetic 14.03-MeV (DT) IRF affects the inferred magnitude of the ground state slightly, but barely affects the inferred width of this state. The inferred ⁵He mass distributions are shown in Fig. 1.

This conclusion concerning the 14.03-MeV IRF is, however, only applicable for this specific detector and this specific combination of nuclear states. It is not possible to know whether any monoenergetic IRF would be an acceptable approximation for the energy-dependent IRF unless the widths and mean energies of the relevant nuclear states are already relatively well known. The use of a monoenergetic IRF to approximate the energy-dependent IRF is therefore not recommended for use with experimental data that spans a wide range of energies, especially if the analysis in question attempts to infer parameters of nuclear states that are currently poorly understood or parameters related to complicated combinations of nuclear states. The use of an energy-dependent IRF is most essential for the analysis of nuclear states with smaller widths, especially if (1) there are several states of relatively narrow widths spread across a wide range of energies, (2) there are several nuclear states located at low energies, and/or (3) there are several relatively sharp features in the nTOF data. Neutron spectra related to backscattered neutrons produced in cryogenic DT experiments as well as neutron spectra produced from inelastic reactions between DT neutrons and ⁷Li are two such applications for which analyses of recent OMEGA data are underway.

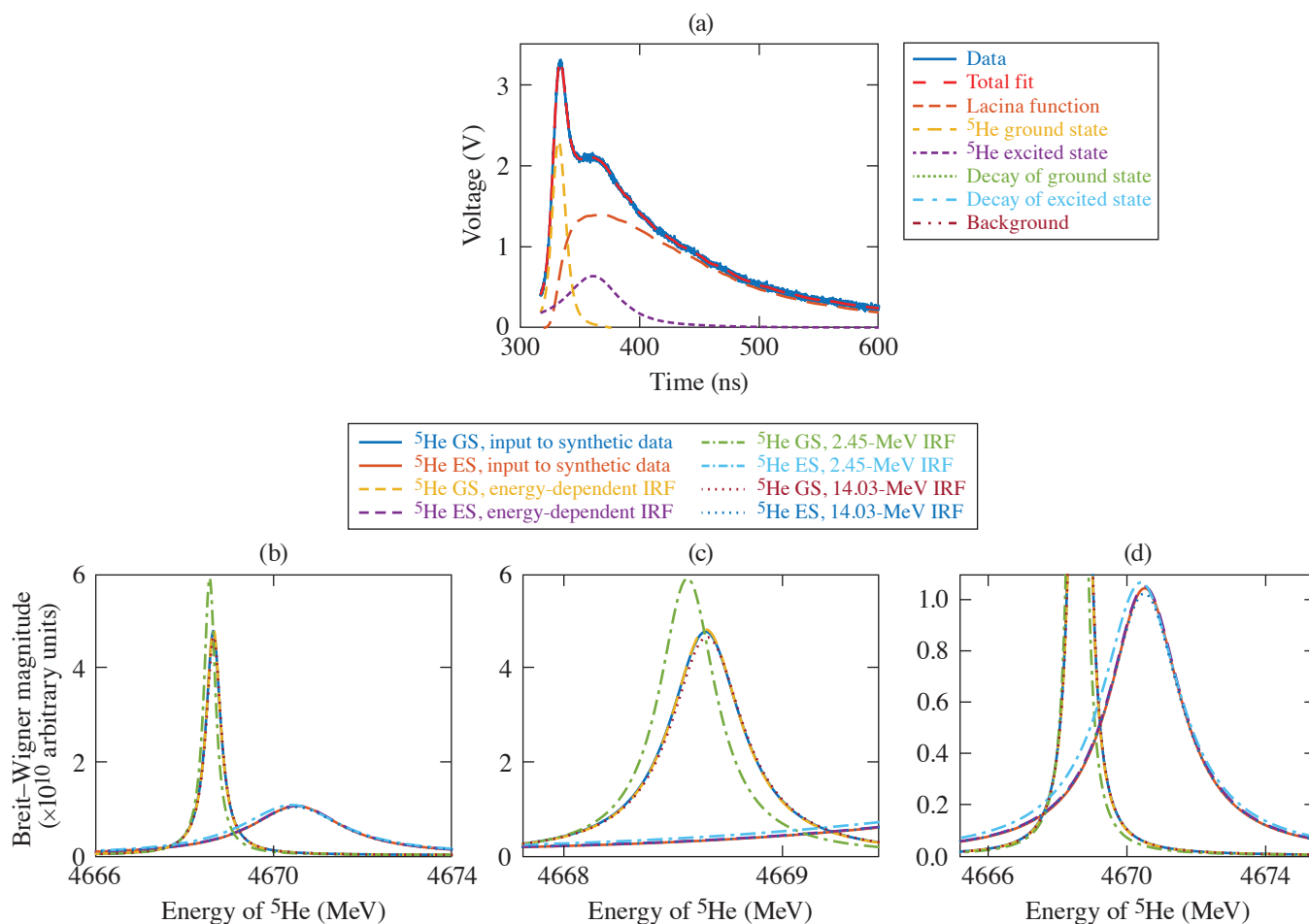


Figure 1

(a) The synthetic TT data and an example of the components of the forward fit are shown along with the inferred ${}^5\text{He}$ mass distributions. (b) The total mass distribution is shown along with (c) two close views of the inferred ground state and (d) the inferred first excited state. The forward fit with the energy-dependent IRF infers the mean energies, width, and magnitudes of the input mass distributions to within a few percent. There is little change to the inferred first excited state regardless of the choice of IRF because it is very wide (2.5 MeV). There is >20% change to the inferred ground state width when the 2.45-MeV monoenergetic IRF is used, but little change when the 14.03-MeV IRF is used. This result is an artifact of this combination of nuclear states and this specific detector setup, as there is only a 300-ps difference between the 8.5-MeV IRF (i.e., the approximate neutron energy where the ${}^5\text{He}$ ground state is located) and the 14.03-MeV IRF for this detector.

This material is based upon work supported by the Department of Energy National Nuclear Security Administration under Award Number DE-NA0003856, the University of Rochester, and the New York State Energy Research and Development Authority.

1. R. Hatarik *et al.*, *J. Appl. Phys.* **118**, 184502 (2015).
2. X-5 Monte Carlo Team, Los Alamos National Laboratory, Los Alamos, NM, Report LA-UR-03-1987 (2008).
3. E. P. Hartouni *et al.*, *Rev. Sci. Instrum.* **87**, 11D841 (2016).
4. Z. L. Mohamed *et al.*, *J. Appl. Phys.* **128**, 214501 (2020).

Parametric Amplification of Spectrally Incoherent Signals

C. Dorrer

Laboratory for Laser Energetics, University of Rochester

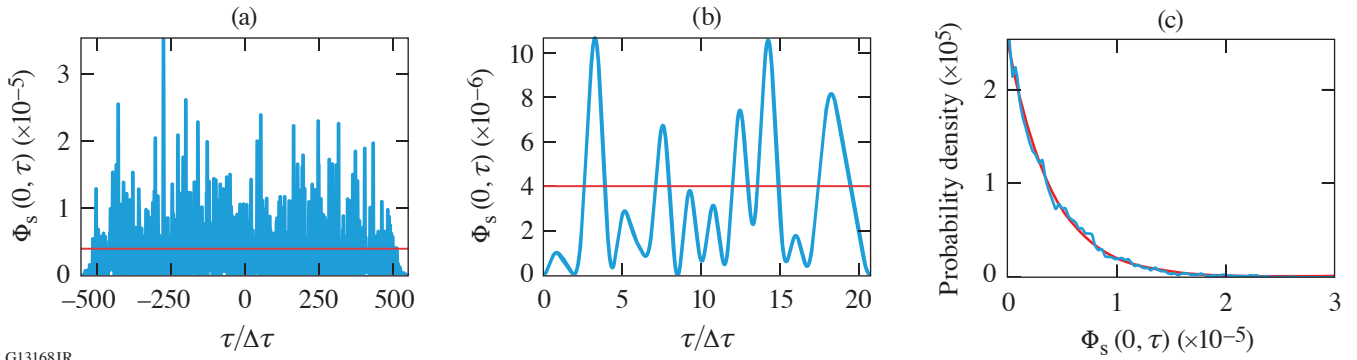
Optical parametric amplifiers (OPA's) compare favorably with laser amplifiers in terms of spectral coverage and broadband operation. Their properties, and in particular the efficiency of the energy transfer between the pump and the signal, have been extensively studied for a spectrally coherent signal,^{1,2} but there are no complete studies of parametric amplification for spectrally incoherent pulses. These pulses are highly relevant to the mitigation of laser–plasma instabilities in high-energy laser–matter interactions.^{3–6} They are the basis for the fourth-generation laser for ultrabroadband experiments (FLUX) currently being built at LLE, where three stages of parametric amplifiers will amplify spectrally incoherent broadband signals. A framework supporting OPA simulations using normalized equations is developed and used to analyze OPA operation with a spectrally incoherent signal, in particular amplification performance and statistical properties of the amplified signal, showing the interplay between OPA properties and initial seeding conditions. These simulations are in agreement with an experimental demonstration of optical parametric amplification with various spectrally incoherent signals.⁷

A set of normalized equations is developed to describe the amplification of a spectrally incoherent signal with coherence time $\Delta\tau$ by a monochromatic pump at a constant intensity $I_{p,0}$. The three-wave nonlinear mixing equations in the absence of group-velocity dispersion² can be normalized into

$$\begin{aligned} \frac{\partial A_s}{\partial z} + \frac{1}{v_s} \frac{\partial A_s}{\partial t} &= -j \frac{\omega_s d_{\text{eff}}}{cn_s} A_i^* A_p \Rightarrow \frac{\partial a_s}{\partial Z} = -j a_i^* a_p, \\ \frac{\partial A_i}{\partial z} + \frac{1}{v_i} \frac{\partial A_i}{\partial t} &= -j \frac{\omega_i d_{\text{eff}}}{cn_i} A_s^* A_p \Rightarrow \frac{\partial a_i}{\partial Z} + \frac{\delta_i}{\Gamma} \frac{\partial a_i}{\partial \tau} = -j a_s^* a_p, \\ \frac{\partial A_p}{\partial z} + \frac{1}{v_p} \frac{\partial A_p}{\partial t} &= -j \frac{\omega_p d_{\text{eff}}}{cn_p} A_s A_i \Rightarrow \frac{\partial a_p}{\partial Z} + \frac{\delta_p}{\Gamma} \frac{\partial a_p}{\partial \tau} = -j a_s a_i. \end{aligned} \quad (1)$$

The fields of the pump A_p , signal A_s , and idler A_i , as a function of time t and longitudinal position z , are normalized according to $a_s = A_s \sqrt{\varepsilon_0 n_s c \omega_p / 2 I_{p,0} \omega_s}$, $a_i = A_i \sqrt{\varepsilon_0 n_i c \omega_p / 2 I_{p,0} \omega_i}$, and $a_p = A_p \sqrt{\varepsilon_0 n_p c / 2 I_{p,0}}$. The OPA is characterized by the temporal walk-off of the idler and pump relative to the signal, δ_i and δ_p , and the commonly used nonlinear coefficient $\Gamma = \sqrt{2 d_{\text{eff}}^2 \omega_1 \omega_2 I_{p,0} / c^3 \varepsilon_0 n_s n_i n_p}$ related to its small-signal gain.²

The quantities $\Phi_s = |a_s|^2 = I_s \omega_p / I_{p,0} \omega_s$, $\Phi_i = |a_i|^2 = I_i \omega_p / I_{p,0} \omega_i$, and $\Phi_p = |a_p|^2 = I_p / I_{p,0}$ are the ratios of the photon flux for the signal, idler, and pump, respectively, at a given time and position to the input-pump photon flux. For a monochromatic signal, the increase in Φ_s and Φ_i during amplification are equal and reach a limit value equal to 1 at full pump depletion (Manley–Rowe relations). The normalized equations allow for general simulations over the properties of the crystal and initial conditions (signal coherence time and input relative energy of the signal and pump), highlighting their impact on the amplification of a spectrally incoherent signal such as the one presented in Fig. 1, which has the expected negative exponential probability density function (pdf). Such a signal, with an initial average photon flux of 4×10^{-6} , leads to pump saturation in an OPA with a small-signal gain equal to 10^6 .



G13168JR

Figure 1

Photon flux ratio for the signal (blue curve) as a function of time normalized to the coherence time over (a) the entire pulse and (b) a time range corresponding to 20 coherence times, where the red line represents the time-averaged photon flux ratio $\Phi_{s,0} = 4 \times 10^{-6}$. (c) Probability density function of the input signal (blue curve) and negative exponential with the same average value (red curve).

An OPA with a small-signal gain equal to 10^6 and no significant idler-signal temporal walk-off (e.g., type-I phase matching close to spectral degeneracy, where the signal wavelength is approximately twice the pump wavelength) is first considered. In the undepleted-pump regime (low signal average flux, $\Phi_{s,0} = 4 \times 10^{-7}$), the amplified signal is proportional to the input signal and maintains a negative-exponential pdf [Fig. 2(a)]. With higher pump depletion [$\Phi_{s,0} = 1.26 \times 10^{-6}$, Fig. 2(b)], at low pump-signal temporal walk-off relative to the signal coherence time stationarity of the signal relative to the pump imposes $\Phi_s < 1$. In longer

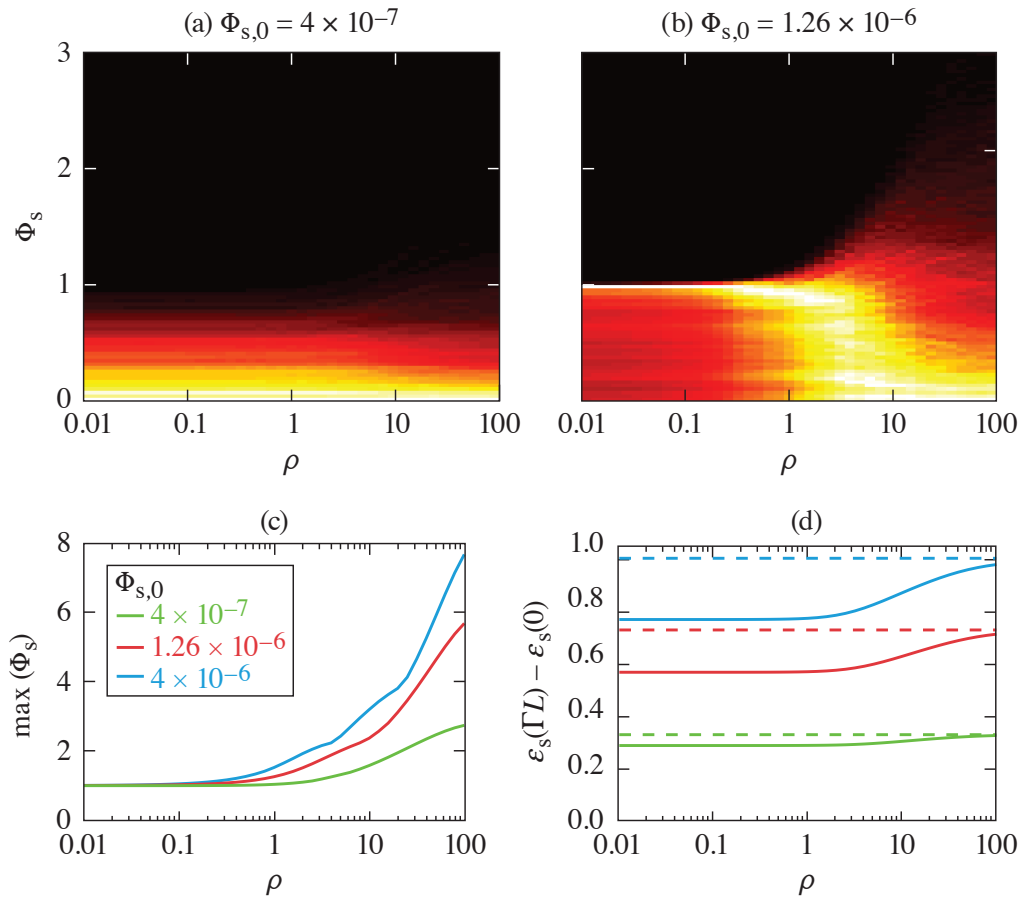


Figure 2

Probability density histograms of the amplified signal as a function of the pump-signal temporal walk-off normalized to the signal coherence time $\rho = \delta_p/\Delta\tau$ in (a) the undepleted-pump regime and (b) with some pump depletion. [(c),(d)] The highest values of the signal photon flux and energy increase as a function of ρ for three depletion conditions.

G13230JR

crystals ($\rho > 1$), however, the signal extracts energy from various temporal slices of the pump, allowing for Φ_s much larger than 1 at some particular times [Figs. 2(b) and 2(c)] and a slight increase in the extracted energy [Fig. 2(d)]. While the pdf is expected to be sharply peaked below 1 at small temporal walk-off, it follows a negative exponential function at large temporal walk-off.

A nonzero idler-signal temporal walk-off limits the amplification efficiency when the signal and idler are relatively shifted by a delay larger than the coherence time $\Delta\tau$, i.e., when $\delta_i L > \Delta\tau$, where L is the crystal length, as indicated by vertical dashed lines on Fig. 3(a) for $\delta_i = \delta_p/10$ and $\delta_i = \delta_p$. Considering that the signal bandwidth is inversely proportional to its coherence time, the energy decrease is fundamentally linked to the OPA phase mismatch, $\delta_i L/\Delta\tau$, as confirmed by the calculated relative bandwidth [Fig. 3(b)]. Spectrally incoherent signals offer an intuitive time-domain picture of the OPA phase mismatch, which is most often described in the spectral domain.

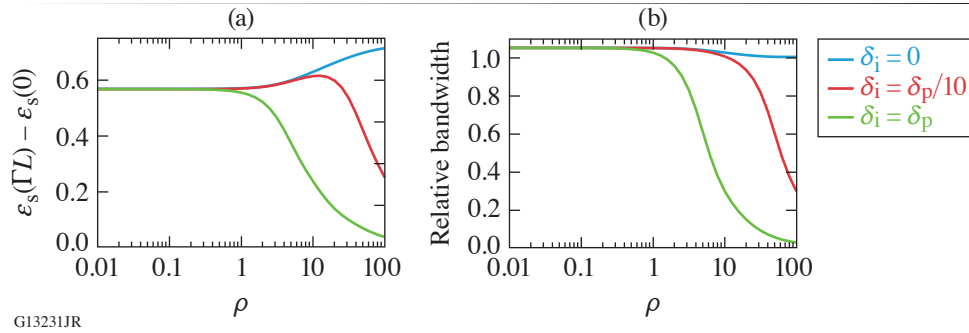


Figure 3

(a) Extracted energy as a function $\rho = \delta_p/\Delta\tau$ for three different ratios δ_i/δ_p . (b) Bandwidth of the amplified signal relative to the initial bandwidth.

Simulations performed with normalized equations are in excellent agreement with simulations that take into account the full dispersion properties of specific nonlinear crystals (BBO, LBO, DKDP). In particular, broadband operation is observed in type-I crystals at spectral degeneracy, while the idler-signal temporal walk-off limits the OPA efficiency when operating away from degeneracy or in type-II crystals.

This material is based upon work supported by the Department of Energy National Nuclear Security Administration under Award Number DE-NA0003856, the University of Rochester, and the New York State Energy Research and Development Authority.

1. R. A. Baumgartner and R. Byer, *IEEE J. Quantum Electron.* **15**, 432 (1979).
2. G. Cerullo and S. De Silvestri, *Rev. Sci. Instrum.* **74**, 1 (2003).
3. J. J. Thomson and J. I. Karush, *Phys. Fluids* **17**, 1608 (1974).
4. S. P. Obenschain, N. C. Luhmann, and P. T. Greiling, *Phys. Rev. Lett.* **36**, 1309 (1976).
5. J. P. Palastro *et al.*, *Phys. Plasmas* **25**, 123104 (2018).
6. R. K. Follett *et al.*, *Phys. Plasmas* **26**, 062111 (2019).
7. C. Dorrer, E. M. Hill, and J. D. Zuegel, *Opt. Express* **28**, 451 (2020).

Comparison of the Laser-Induced–Damage Threshold in Single-Layer Optical Films Measured at Different Facilities

L. Lamaignère,¹ A. Ollé,¹ M. Chorel,¹ N. Roquin,¹ A. A. Kozlov,² B. N. Hoffman,² J. B. Oliver,² S. G. Demos,² L. Gallais,³ R. A. Negres,⁴ and A. Melninkaitis⁵

¹Commissariat à l'énergie atomique et aux énergies alternatives, CESTA

²Laboratory for Laser Energetics, University of Rochester

³Aix-Marseille University, CNRS, Centrale Marseille, Institut Fresnel

⁴National Ignition Facility and Photon Sciences, Lawrence Livermore National Laboratory

⁵Laser Research Center, Vilnius University

The laser-induced–damage thresholds (LIDT's) of two different coatings were measured in a round-robin experiment involving five well-equipped damage-testing facilities. Investigations were conducted at a wavelength of 1 μm in the subpicosecond-pulse-duration regime with different configurations in terms of polarization, angle of incidence, and environment (air versus vacuum). The results of this round-robin damage-testing effort revealed significant differences between facilities.

The standardization and comparison of laser-damage protocols and results are essential prerequisites for development and quality control of large optical components used in high-power laser facilities. This may be critical for the development of next-generation laser systems or even to improve the operational envelope of current-generation, large-aperture laser systems such as OMEGA EP¹ and PETAL.² Although the damage-initiation process is due to defects, and therefore the damage behavior of a material is best described by a damage probability curve, the damage threshold under subpicosecond laser excitation using a small area beam for testing is characterized by a narrow range of fluences in the transition from 0% to 100% probability for laser damage. This threshold behavior allows one to measure the damage threshold with great precision (which can be considered to be “deterministic”). This in turn simplifies a direct comparison of LIDT measurements from different facilities in order to explore how systematic factors in the measurement method can affect the result, aiding in the development of standardized damage-testing protocols.

The objective of this work was to compare results of LIDT testing of two dielectric materials, HfO_2 and SiO_2 , in the form of single layers tested at five different laser facilities. The facilities utilized very similar characteristics such as similar wavelengths (around 1 μm), pulse duration (0.8 ps), and beam size. The tests were based on the protocol described by the ISO 21254 Standard.³ The hafnia (HfO_2) and silica (SiO_2) single layers selected for these tests are common materials used in multilayer dielectric optical components employed in short-pulse laser systems as high- and low-refractive-index materials, respectively. All test substrates for a given coating type were produced during a single coating deposition (and therefore are considered identical) and have been deposited by electron-beam evaporation with ion assistance on BK7 substrates. Testing was performed in four configurations with respect to incidence angle and beam polarization ($0^\circ p$ polarization, $45^\circ p$ polarization, $0^\circ s$ polarization, and $45^\circ s$ polarization). The layer thickness of the hafnia and silica layers was 149.9 and 194.3 nm, respectively. The results reported in this summary obtained from five different facilities (see author affiliations) are presented anonymously in the form Lab A, B, C, D, E (for laboratory A, B, C, D, and E). Following the presentation of the raw results of LIDT measurements, we examine the various parameters, which are hypothesized to be the sources for the observed discrepancies between these measurements.

The values of the refractive index and thickness were used to calculate the electric-field–intensity distribution within each single layer using OptiLayer software⁴ and the maximum enhancement of the electric-field intensity (EFI_{max}) in the layer was

determined for each testing configuration. This EFI_{max} value was used in combination with the measured LIDT ($LIDT_{exp}$) in each material and testing configuration to estimate the “intrinsic” LIDT ($LIDT_{int}$) for the two single layers using Eq. (1):

$$LIDT_{int} = LIDT_{exp} \times EFI_{max}. \tag{1}$$

Results are given in Table I for HfO_2 and SiO_2 single layers. Only results obtained in an air environment are compared since only two of the five testing facilities had the capability for testing in vacuum.

Table I: Intrinsic LIDT’s ($LIDT_{int}$) for HfO_2 and SiO_2 monolayers estimated by means of relation (1) and raw damage test experimental data. Thresholds are given in terms of energy density (fluence) in J/cm^2 .

	HfO ₂ monolayer						SiO ₂ monolayer					
	p polarization		s polarization		LIDT _{int}		p polarization		s polarization		LIDT _{int}	
	0°	45°	0°	45°	mean	σ	0°	45°	0°	45°	mean	σ
Lab A	1.94	2.06	–	2.04	2.01	0.04	3.03	2.99	–	2.93	2.99	0.03
Lab B	2.13	1.87	2.17	out of range	2.06	0.09	2.96	out of range	3.09	out of range	3.02	0.07
Lab C	1.54	1.37	1.41	1.36	1.42	0.04	2.00	2.15	2.01	2.05	2.05	0.04
Lab D	1.63	1.39	–	1.60	1.54	0.07	2.03	2.18	–	2.15	2.12	0.05
Lab E	1.64	1.48	–	1.48	1.53	0.09	Not tested					

The round-robin LIDT measurements of two dielectric single layers showed significant differences. Deviations of the order of 21% were obtained, much greater than the absolute measurement uncertainties on the facilities estimated to be at least 10%. This is an unexpected and highly undesirable result. LIDT determination in this pulse-length regime should be straightforward, and results should be comparable. An analysis of the various contributors involved in the measurement of damage thresholds shows, however, that differences of 20% are nevertheless plausible. The hypothesized principal mechanism to explain such deviations must be explored in future work to resolve this difficulty in determining damage-threshold measurements in the short-pulse regime. We suggest that it is of fundamental importance to pay increased attention to specific metrology:

- Acquire accurate beam spatial-profile measurements with special attention to the sensor noise determination in the case of a small beam on a large sensor window.
- The problem of nonlinear beam propagation affecting the experimental measurements, mainly the beam profile, must be considered.
- Experimental conditions must be perfectly known and controlled as, for example, hygrometry and/or environment.
- Precise knowledge of the temporal intensity profile is also imperative.

This material is based in part upon work supported by the Department of Energy National Nuclear Security Administration under Award Number DE-NA0003856, the University of Rochester, and the New York State Energy Research and Development Authority. Part of this work was performed under the auspices of the U.S. Department of Energy (DOE) by Lawrence Livermore National Laboratory under Contract DE-AC52-07NA27344.

1. L. J. Waxer *et al.*, Opt. Photonics News **16**, 30 (2005).
2. N. Blanchot *et al.*, Opt. Express **25**, 16,957 (2017).
3. ISO 21254-1:2011- 21254-4:2011(E), “Lasers and Laser-Related Equipment—Test Methods for Laser-Induced Damage Threshold”—Parts 1–4 (International Organization for Standardization, Geneva, Switzerland, 2011), pp. 1–5.
4. A. V. Tikhonravov and M. K. Trubetskov, OptiLayer Thin Film Software, Optilayer Ltd., <http://www.optilayer.com>.

The 12th Omega Laser Facility Users Group Workshop

M. S. Wei and S. F. B. Morse

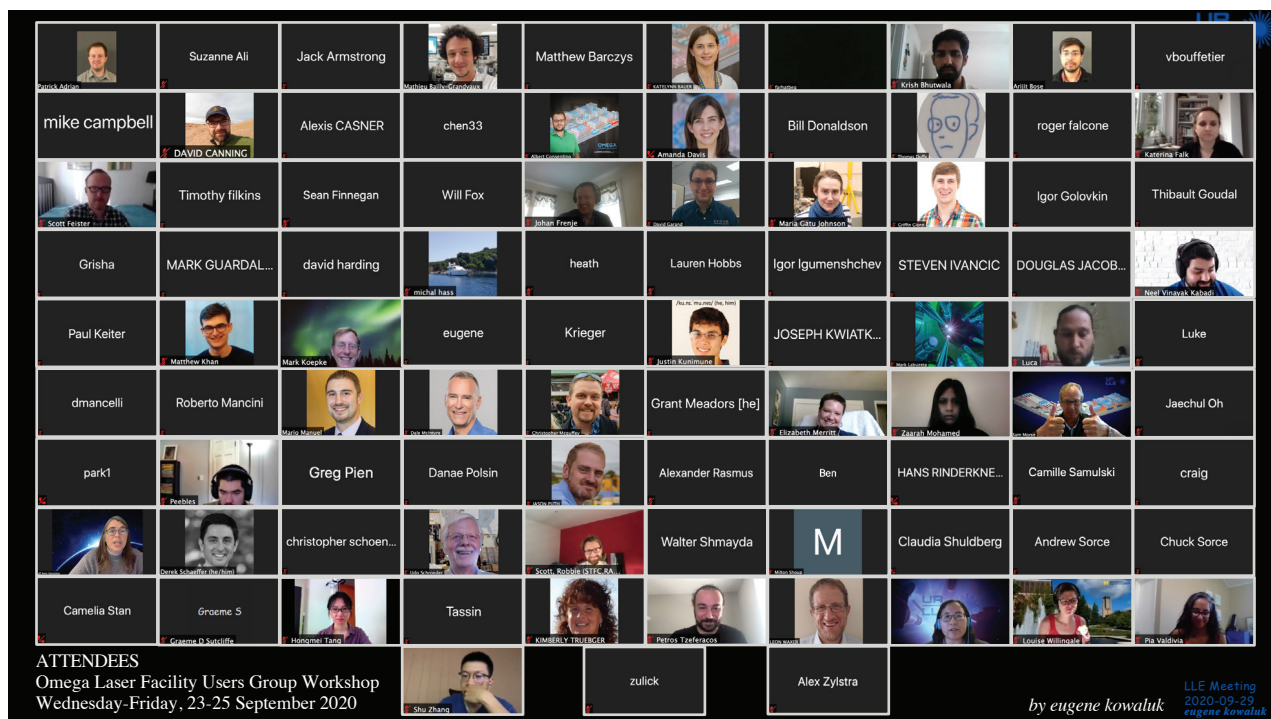
Laboratory for Laser Energetics, University of Rochester

LLE hosted a virtual meeting for the Omega Laser Facility User Group (OLUG) 23–25 September 2020 with more than 90 participants from 27 institutions (see Fig. 1). The objective of this meeting was the development of Findings and Recommendations (F&R's) to improve facility capabilities and user experience/effectiveness. The first day of the meeting began with two facility presentations: “Omega Facility Updates” (including LLE responses to the 2019 OLUG F&R's) and “Omega RemotePI Operation,” (a comprehensive description of the RemotePI capability developed during the pandemic lockdown in Q3). Over the three days (two hours each day), OLUG members discussed and developed a list of 23 new F&R's. A few highlights include:

- Automated online access to post-processed neutronic data through the Omega operation webpage.
- A dedicated gas-jet nozzle characterization station to measure the plasma density for each specific nozzle used to create targets for experiments.
- Enhanced VISAR (velocity interferometer system for any reflector)/SOP (streaked optical pyrometer) capability, including its implementation in an additional ten-inch manipulator (TIM) on OMEGA EP to allow simultaneous shock pressure and x-ray diffraction measurements.
- A new TIM-based particle spectrometer that works in an intense x-ray background.
- Enhanced pulse-shaping capability to flexibly control/correct the as-shot laser pulse shapes on OMEGA.
- Longer pulse durations on OMEGA EP (UV beams) for studying photoionized plasmas, laboratory astrophysics, and high-energy-density hydrodynamics.
- A dedicated short-pulse beam (i.e., not sourced from OMEGA EP) on OMEGA for ultrafast diagnostics and short-pulse interaction physics in the OMEGA chamber (a longer-term development project).

On the last day of the meeting, Mingsheng Wei gave an update on the Omega Basic Science Program and Ann Satsangi described the NNSA perspectives and gave an update on Academic Programs.

The next OLUG Workshop with a full meeting agenda including poster sessions will be held virtually 27–30 April 2021.



U2671JR

Figure 1
2020 OLUG virtual meeting attendees.

FY20 Q4 Laser Facility Report

J. Puth, M. Labuzeta, D. Canning, and R. T. Janezic

Laboratory for Laser Energetics, University of Rochester

During the fourth quarter of FY20, the Omega Laser Facility conducted 368 target shots on OMEGA and 266 target shots on OMEGA EP for a total of 624 target shots (see Tables I and II). OMEGA averaged 10.8 target shots per operating day, averaging 91.9% Availability and 96.7% Experimental Effectiveness. OMEGA EP averaged 8.3 target shots per operating day, averaging 93.3% Availability and 94.9% Experimental Effectiveness.

Table I: OMEGA Laser System target shot summary for Q4 FY20.

Program	Laboratory	Planned Number of Target Shots	Actual Number of Target Shots
ICF	LLE	104.5	99
	LANL	11	11
	LLNL	11	8
ICF Subtotal		126.5	118
HED	LLE	44	47
	LLNL	27.5	22
	SNL	11	9
HED Subtotal		82.5	78
LBS	LLE	22	23
	LLNL	22	25
LBS Subtotal		44	48
AIBS		33	38
NLUF		11	10
RAL		11	12
NLUF		11	10
LDRD		11	9
Calibration	LLE	0	45
Grand Total		330	368

Table II: OMEGA EP Facility Target Shot Summary for Q4 FY20.

Program	Laboratory	Planned Number of Target Shots	Actual Number of Target Shots
ICF	LLE	45.5	64
	LLNL	28	44
ICF Subtotal		73.5	108
HED	LANL	14	13
	LLE	7	7
	LLNL	42	44
HED Subtotal		63	64
LBS	LLNL	14	22
NLUF		28	28
AIBS		14	19
LaserNetUS		14	22
Calibration	LLE	0	3
Grand Total		206.5	266

A prototype alignment package in the stage-F diagnostics area featuring a modern digital camera was installed on the OMEGA laser. This upgrade will improve the resolution of the alignment and prevent operational delays associated with the aging analog components. The design has been validated, and all 60 beams will be upgraded over the upcoming six months.

Publications and Conference Presentations

Publications

- M. Bailly-Grandvaux, D. Kawahito, C. McGuffey, J. Strehlow, B. Edghill, M. S. Wei, N. Alexander, A. Haid, C. Brabetz, V. Bagnoud, R. Hollinger, M. G. Capeluto, J. J. Rocca, and F. N. Beg, "Ion Acceleration from Microstructured Targets Irradiated by High-Intensity Picosecond Laser Pulses," *Phys. Rev. E* **102**, 021201(R) (2020).
- K. L. Baker, C. A. Thomas, D. T. Casey, M. Hohenberger, S. Khan, B. K. Spears, O. L. Landen, R. Nora, D. T. Woods, J. L. Milovich, R. L. Berger, D. Strozzi, C. Weber, D. Clark, O. A. Hurricane, D. A. Callahan, A. L. Kritcher, B. Bachmann, L. R. Benedetti, R. Bionta, P. M. Celliers, D. Fittinghoff, C. Goyon, R. Hatarik, N. Izumi, M. Gatu Johnson, G. Kyrala, T. Ma, K. Meaney, M. Millot, S. R. Nagel, P. K. Patel, D. Turnbull, P. L. Volegov, C. Yeaman, and C. Wilde, "Hotspot Parameter Scaling with Velocity and Yield for High-Adiabatic Layered Implosions at the National Ignition Facility," *Phys. Rev. E* **102**, 023210 (2020).
- D. H. Barnak, J. R. Davies, J. P. Knauer, and P. M. Kozlowski, "Soft X-Ray Spectrum Unfold of K-Edge Filtered X-Ray Diode Arrays Using Cubic Splines," *Rev. Sci. Instrum.* **91**, 073102 (2020).
- K. A. Bauer, M. Heimbueger, J. Kwiatkowski, S. Sampat, L. J. Waxer, E. C. Cost, J. H. Kelly, V. Kobilansky, S. F. B. Morse, D. Nelson, D. Weiner, G. Weselak, and J. Zou, "Optical Characterization of the On-Target OMEGA Focal Spot at High Energy Using the Full-Beam In-Tank Diagnostic," *Appl. Opt.* **59**, 7994 (2020).
- P. T. Campbell, C. A. Walsh, B. K. Russell, J. P. Chittenden, A. Crilly, G. Fiksel, P. M. Nilson, A. G. R. Thomas, K. Krushelnick, and L. Willingale, "Magnetic Signatures of Radiation-Driven Double Ablation Fronts," *Phys. Rev. Lett.* **125**, 145001 (2020).
- Y.-H. Chen, J. R. Peterson, L. A. Johnson, T. G. Jones, B. Hafizi, A. B. Stamm, A. C. Ting, J. P. Palastro, M. H. Helle, and D. Kaganovich, "Nonlinear Underwater Propagation of Picosecond Ultraviolet Laser Beams," *Opt. Lett.* **45**, 4344 (2020).
- W. A. Farmer, C. Bruulsema, G. F. Swadling, M. W. Sherlock, M. D. Rosen, W. Rozmus, D. H. Edgell, J. Katz, B. B. Pollock, and J. S. Ross, "Validation of Heat Transport Modeling Using Directly Driven Beryllium Spheres," *Phys. Plasmas* **27**, 082701 (2020).
- M. Gatu Johnson, B. M. Haines, P. J. Adrian, C. Forrest, J. A. Frenje, V. Yu. Glebov, W. Grimble, R. Janezic, J. P. Knauer, B. Lahmann, F. J. Marshall, T. Michel, F. H. Séguin, C. Stoeckl, and R. D. Petrasso "3D xRAGE Simulation of Inertial Confinement Fusion Implosion with Imposed Mode 2 Laser Drive Asymmetry," *High Energy Density Phys.* **36**, 100825 (2020).
- V. N. Goncharov, I. V. Igumenshchev, D. R. Harding, S. F. B. Morse, S. X. Hu, P. B. Radha, D. H. Froula, S. P. Regan, T. C. Sangster, and E. M. Campbell, "Novel Hot-Spot Ignition Designs for Inertial Confinement Fusion with Liquid-Deuterium-Tritium Spheres," *Phys. Rev. Lett.* **125**, 065001 (2020).
- J. Hinz, V. V. Karasiev, S. X. Hu, M. Zaghoo, D. Mejía-Rodríguez, S. B. Trickey, and L. Calderín, "Fully Consistent Density Functional Theory Determination of the Insulator-Metal Transition Boundary in Warm Dense Hydrogen," *Phys. Rev. Res.* **2**, 032065(R) (2020).
- B. N. Hoffman, A. A. Kozlov, N. Liu, H. Huang, J. B. Oliver, A. L. Rigatti, T. J. Kessler, A. A. Shestopalov, and S. G. Demos, "Mechanisms of Picosecond Laser-Induced Damage in Common Multilayer Dielectric Gratings," *Opt. Express* **28**, 24,928 (2020).
- A. L. Kritcher, D. C. Swift, T. Döppner, B. Bachmann, L. X. Benedict, G. W. Collins, J. L. DuBois, F. Elsner, G. Fontaine, J. A. Gaffney, S. Hamel, A. Lazicki, W. R. Johnson, N. Kostinski, D. Kraus, M. J. MacDonald, B. Maddox, M. E. Martin, P. Neumayer, A. Nikroo, J. Nilsen, B. A. Remington, D. Saumon, P. A. Sterne, W. Sweet, A. A. Correa, H. D. Whitley, R. W. Falcone, and S. H. Glenzer, "A Measurement of the Equation of State of Carbon Envelopes of White Dwarfs," *Nature* **584**, 51 (2020).

A. V. Maximov, J. G. Shaw, and J. P. Palastro, "Nonlinear Transmission of Laser Light Through Coronal Plasma Due to Self-Induced Incoherence," *Phys. Rev. E* **102**, 023205 (2020).

R. Paul, S. X. Hu, V. V. Karasiev, S. A. Bonev, and D. N. Polsin, "Thermal Effects on the Electronic Properties of Sodium Electride Under High Pressures," *Phys. Rev. B* **102**, 094103 (2020).

A. Pineau, B. Chimier, S. X. Hu, and G. Duchateau, "Modeling the Electron Collision Frequency During Solid-to-Plasma Transition of Polystyrene Ablator for Direct-Drive Inertial Confinement Fusion Applications," *Phys. Plasmas* **27**, 092703 (2020).

M. Sharpe, W. T. Shmayda, and K. Glance, "Measurement of Palladium Hydride and Palladium Deuteride Isotherms Between 130 K and 393 K," *Fusion Sci. Technol.* **76**, 642 (2002).

D. B. Sinars, M. A. Sweeney, C. S. Alexander, D. J. Ampleford, T. Ao, J. P. Apruzese, C. Aragon, D. J. Armstrong, K. N. Austin, T. J. Awe, A. D. Baczewski, J. E. Bailey, K. L. Baker, C. R. Ball, H. T. Barclay, S. Beatty, K. Beckwith, K. S. Bell, J. F. Benage, Jr., N. L. Bennett, K. Blaha, D. E. Bliss, J. J. Boerner, C. J. Bourdon, B. A. Branch, J. L. Brown, E. M. Campbell, R. B. Campbell, D. G. Chacon, G. A. Chandler, K. Chandler, P. J. Christenson, M. D. Christison, E. B. Christner, R. C. Clay III, K. R. Cochrane, A. P. Colombo, B. M. Cook, C. A. Coverdale, M. E. Cuneo, J. S. Custer, A. Dasgupta, J.-P. Davis, M. P. Desjarlais, D. H. Dolan III, J. D. Douglass, G. S. Dunham, S. Duwal, A. D. Edens, M. J. Edwards, E. G. Evstatiev, B. G. Farfan, J. R. Fein, E. S. Field, J. A. Fisher, T. M. Flanagan, D. G. Flicker, M. D. Furnish, B. R. Galloway, P. D. Gard, T. A. Gardiner, M. Geissel, J. L. Giuliani, M. E. Glinksy, M. R. Gomez, G. P. Grim, K. D. Hahn, T. A. Hail, N. D. Hamlin, J. H. Hammer, S. B. Hansen, H. L. Hanshaw, E. C. Harding, A. J. Harvey-Thompson, D. Headley, M. C. Herrmann, M. H. Hess, C. Highstrete, O. A. Hurricane, B. T. Hutsel, C. A. Jennings, O. M. Johns, D. Johnson, M. D. Johnston, B. M. Jones, M. C. Jones, P. A. Jones, P. E. Kalita, R. J. Kamm, J. W. Kellogg, M. L. Kiefer, M. W. Kimmel, P. F. Knapp, M. D. Knudson, A. Kreft, G. R. Laity, P. W. Lake, D. C. Lamppa,

W. L. Langston, J. S. Lash, K. R. LeChien, J. J. Leckbee, R. J. Leeper, G. T. Leifeste, R. W. Lemke, W. Lewis, S. A. Lewis, G. P. Loisel, Q. M. Looker, A. J. Lopez, D. J. Lucero, S. A. MacLaren, R. J. Magyar, M. A. Mangan, M. R. Martin, T. R. Mattsson, M. K. Matzen, A. J. Maurer, M. G. Mazarakis, R. D. McBride, H. S. McLean, C. A. McCoy, G. R. McKee, J. L. McKenney, A. R. Miles, J. A. Mills, M. D. Mitchell, N. W. Moore, C. E. Myers, T. Nagayama, G. Natoni, A. C. Owen, S. Patel, K. J. Peterson, T. D. Pointon, J. L. Porter, A. J. Porwitzky, S. Radovich, K. S. Raman, P. K. Rambo, W. D. Reinhart, G. K. Robertson, G. A. Rochau, S. Root, D. V. Rose, D. C. Rovang, C. L. Ruiz, D. E. Ruiz, D. Sandoval, M. E. Savage, M. E. Sceiford, M. A. Schaeuble, P. F. Schmit, M. S. Schollmeier, J. Schwarz, C. T. Seagle, A. B. Sefkow, D. B. Seidel, G. A. Shipley, J. Shores, L. Shulenburg, S. C. Simpson, S. A. Slutz, I. C. Smith, C. S. Speas, P. E. Specht, M. J. Speir, D. C. Spencer, P. T. Springer, A. M. Steiner, B. S. Stolfus, W. A. Stygar, J. Ward Thornhill, J. A. Torres, J. P. Townsend, C. Tyler, R. A. Vesey, P. E. Wakeland, T. J. Webb, E. A. Weinbrecht, M. R. Weis, D. R. Welch, J. L. Wise, M. Wu, D. A. Yager-Elorriaga, A. Yu, and E. P. Yu, "Review of Pulsed Power-Driven High Energy Density Physics Research on Z at Sandia," *Phys. Plasmas* **27**, 070501 (2020).

S. Tochitsky, A. Pak, F. Fiuza, D. Haberberger, N. Lemos, A. Link, D. H. Froula, and C. Joshi, "Laser-Driven Collisionless Shock Acceleration of Ions from Near-Critical Plasmas," *Phys. Plasmas* **27**, 083102 (2020).

S. Zhang and S. X. Hu, "Species Separation and Hydrogen Streaming upon Shock Release from Polystyrene Under Inertial Confinement Fusion Conditions," *Phys. Rev. Lett.* **125**, 105001 (2020).

A. B. Zylstra, R. S. Craxton, J. R. Rygg, C.-K. Li, L. Carlson, M. J.-E. Manuel, E. L. Alfonso, M. Mauldin, L. Gonzalez, K. Youngblood, E. M. Garcia, L. T. Browning, S. Le Pape, N. Candeias Lemos, B. Lahmann, M. Gatu Johnson, H. Sio, and N. Kabadi, "Saturn-Ring Proton Backlighters for the National Ignition Facility," *Rev. Sci. Instrum.* **91**, 093505 (2020).

Forthcoming Publications

K. S. Anderson, C. J. Forrest, O. M. Mannion, F. J. Marshall, R. C. Shah, D. T. Michel, J. A. Marozas, P. B. Radha, D. Edgell, R. Epstein, V. N. Goncharov, J. P. Knauer, M. Gatun Johnson, and S. Laffite, "Effect of Cross-Beam Energy Transfer on Target-Offset Asymmetry in Direct-Drive Inertial Confinement Fusion Implosions," to be published in *Physics of Plasmas*.

D. H. Barnak, M. J. Bonino, P.-Y. Chang, J. R. Davies, E. C. Hansen, D. R. Harding, J. L. Peebles, and R. Betti, "Characterizing Laser Preheat for Laser-Driven Magnetized Liner Inertial Fusion Using Soft X-Ray Emission," to be published in *Physics of Plasmas*.

I. A. Begishev, G. Brent, S. Carey, R. Chapman, I. A. Kulagin, M. H. Romanofsky, M. J. Shoup III, J. D. Zuegel, and J. Bromage, "High-Efficiency, Fifth-Harmonic-Generation of a Joule-Level Neodymium Laser in a Large-Aperture Ammonium Dihydrogen Phosphate Crystal," to be published in *Optics Express*.

E. M. Campbell, T. C. Sangster, V. N. Goncharov, J. D. Zuegel, S. F. B. Morse, C. Sorce, G. W. Collins, M. S. Wei, R. Betti, S. P. Regan, D. H. Froula, C. Dorrer, D. R. Harding, V. Gopalaswamy, J. P. Knauer, R. Shah, O. M. Mannion, J. A. Marozas, P. B. Radha, M. J. Rosenberg, T. J. B. Collins, A. R. Christopherson, A. A. Solodov, D. Cao, J. P. Palastro, R. K. Follett, and M. Farrell, "Direct-Drive Laser Fusion: Status, Plans, and Future," to be published in *Philosophical Transactions of the Royal Society A*.

L. E. Crandall, J. R. Rygg, D. K. Spaulding, T. R. Boehly, S. Brygoo, P. M. Celliers, J. H. Eggert, D. E. Fratanduono, B. J. Henderson, M. F. Huff, R. Jeanloz, A. Lazicki, M. C. Marshall, D. N. Polsin, M. Zaghoo, M. Millot, and G. W. Collins, "Equation of State of CO₂ Shock Compressed to 1 TPa," to be published in *Physical Review Letters*.

B. M. Haines, R. C. Shah, J. M. Smidt, B. J. Albright, T. Cardenas, M. R. Douglas, C. Forrest, V. Yu. Glebov, M. A. Gunderson, C. Hamilton, K. Henderson, Y. Kim, M. N. Lee, T. J. Murphy, J. A. Oertel, R. E. Olson, B. M. Patterson, R. B. Randolph, and D. Schmidt, "The Rate of Development of Atomic Mixing and Temperature Equilibration in Inertial Confinement Fusion Implosions," to be published in *Physics of Plasmas*.

D. R. Harding, M. D. Wittman, N. P. Redden, D. H. Edgell, and J. Ulreich, "Comparison of Shadowgraphy and X-Ray Phase

Contrast Methods for Characterizing a DT Ice Layer in an Inertial Confinement Fusion Target," to be published in *Fusion Science and Technology*.

A. J. Harvey-Thompson, M. R. Weis, D. E. Ruiz, M. S. Wei, A. B. Sefkow, T. Nagayama, E. M. Campbell, J. A. Fooks, M. E. Glinsky, and K. J. Peterson, "The Effect of Laser Entrance Hold Foil Thickness on MagLIF-Relevant Laser Preheat," to be published in *Physics of Plasmas*.

G. W. Jenkins, C. Feng, and J. Bromage, "Overcoming Gas Ionization Limitations with Divided-Pulse Nonlinear Compression," to be published in *Optics Express*.

K. R. P. Kafka, B. N. Hoffman, H. Huang, and S. G. Demos, "Mechanisms of Picosecond Laser-Induced Damage from Interaction with Model Contamination Particles on a High Reflector," to be published in *Optical Engineering*.

D. Kawahito, M. Bailly-Grandvaux, M. Dozières, C. McGuffey, P. Forestier-Colleoni, J. Peebles, J. J. Honrubia, B. Khair, S. Hansen, P. Tzeferacos, M. S. Wei, C. M. Krauland, P. Gourdain, J. R. Davies, K. Matsuo, S. Fujioka, E. M. Campbell, J. J. Santos, D. Batani, K. Bhutwala, S. Zhang, and F. N. Beg, "Fast Electron Transport Dynamics and Energy Deposition in Magnetized, Imploded Cylindrical Plasma," to be published in *Philosophical Transactions of the Royal Society A*.

T. Z. Kosc, H. Huang, T. J. Kessler, R. A. Negres, and S. G. Demos, "Determination of the Raman Polarizability Tensor in the Optically Anisotropic Crystal Potassium Dihydrogen Phosphate and Its Deuterated Analog," to be published in *Scientific Reports*.

C. A. McCoy, S. X. Hu, M. C. Marshall, D. N. Polsin, D. E. Fratanduono, Y. H. Ding, P. M. Celliers, T. R. Boehly, and D. D. Meyerhofer, "Measurement of the Sound Velocity and Grüneisen Parameter of Polystyrene at Inertial Confinement Fusion Conditions," to be published in *Physical Review B*.

B. Militzer, F. González-Cataldo, S. Zhang, H. D. Whitley, D. C. Swift, and M. Millot, "Nonideal Mixing Effects in Warm Dense Matter Studied with First-Principles Computer Simulations," to be published in the *Journal of Chemical Physics*.

D. Ramsey, P. Franke, T. T. Simpson, D. H. Froula, and J. P. Palastro, "Vacuum Acceleration of Electrons in a Dynamic Laser Pulse," to be published in *Physical Review E*.

J. J. Ruby, J. R. Rygg, D. A. Chin, J. A. Gaffney, P. J. Adrian, D. Bishel, C. J. Forrest, V. Yu. Glebov, N. V. Kabadi, P. M. Nilson, Y. Ping, C. Stoeckl, and G. W. Collins, “Constraining Physical Models at Gigabar Pressures,” to be published in *Physical Review E*.

J. J. Ruby, J. R. Rygg, D. A. Chin, J. A. Gaffney, P. J. Adrian, C. J. Forrest, V. Yu. Glebov, N. V. Kabadi, P. M. Nilson, Y. Ping, C. Stoeckl, and G. W. Collins, “Energy Flow in Thin Shell Implosions and Explosions,” to be published in *Physical Review Letters*.

T. T. Simpson, D. Ramsey, P. Franke, N. Vafaei-Najafabadi, D. Turnbull, D. H. Froula, and J. P. Palastro, “Nonlinear Spatiotemporal Control of Laser Intensity,” to be published in *Optics Letters*.

R. Sobolewski, “Optical Detectors and Sensors,” to be published in the *Handbook of Superconducting Materials*.

C. A. Thomas, E. M. Campbell, K. L. Baker, D. T. Casey, M. Hohenberger, A. L. Kritcher, B. K. Spears, S. F. Khan, R. Nora, D. T. Woods, J. L. Milovich, R. L. Berger, D. Strozzi, D. D. Ho, D. Clark, B. Bachmann, L. R. Benedetti, R. Bionta, P. M. Celliers, D. Fittinghoff, G. Grim, R. Hatarik, N. Izumi, G. Kyrala, T. Ma, M. Millot, S. R. Nagel, P. K. Patel, C. Yeamans, A. Nikroo, M. Tabak, M. Gatu Johnson, P. L. Volegov, and S. M. Finnegan, “Deficiencies in Compression and Yield in X-Ray-Driven Implosions,” to be published in *Physics of Plasmas*.

C. A. Thomas, E. M. Campbell, K. L. Baker, D. T. Casey, M. Hohenberger, A. L. Kritcher, B. K. Spears, S. F. Khan, R. Nora, D. T. Woods, J. L. Milovich, R. L. Berger, D. Strozzi, D. D. Ho, D. Clark, B. Bachmann, L. R. Benedetti, R. Bionta, P. M. Celliers, D. N. Fittinghoff, G. Grim, R. Hatarik, N. Izumi, G. Kyrala, T. Ma, M. Millot, S. R. Nagel, P. K. Patel, C. Yeamans, A. Nikroo, M. Tabak, M. Gatu Johnson,

P. Volegov, and S. M. Finnegan, “Experiments to Explore the Influence of Pulse Shaping at the National Ignition Facility,” to be published in *Physics of Plasmas*.

C. A. Thomas, E. M. Campbell, K. L. Baker, D. T. Casey, M. Hohenberger, A. L. Kritcher, B. K. Spears, S. F. Khan, R. Nora, D. T. Woods, J. L. Milovich, R. L. Berger, D. Strozzi, D. D. Ho, D. Clark, B. Bachmann, R. Benedetti, R. Bionta, P. M. Celliers, D. Fittinghoff, G. Grim, R. Hatarik, N. Izumi, G. Kyrala, T. Ma, M. Millot, S. R. Nagel, P. K. Patel, C. Yeamans, A. Nikroo, M. Tabak, M. Gatu Johnson, P. Volegov, and S. M. Finnegan, “Principal Factors in Performance in Indirect-Drive Laser Fusion Experiments,” to be published in *Physics of Plasmas*.

D. Turnbull, A. V. Maximov, D. Cao, A. R. Christopherson, D. H. Edgell, R. K. Follett, V. Gopalaswamy, J. P. Knauer, J. P. Palastro, A. Shvydky, C. Stoeckl, H. Wen, and D. H. Froula, “Impact of Spatiotemporal Smoothing on the Two-Plasmon–Decay Instability,” to be published in *Physics of Plasmas*.

S. Zhang, M. C. Marshall, L. H. Yang, P. A. Sterne, B. Militzer, M. Däne, J. A. Gaffney, A. Shamp, T. Ogitsu, K. Caspersen, A. E. Lazicki, D. Erskine, R. A. London, P. M. Celliers, J. Nilsen, and H. D. Whitley, “Benchmarking Boron Carbide Equation of State Using Computation and Experiment,” to be published in *Physical Review E*.

S. Zhang, H. D. Whitley, and T. Ogitsu, “Phase Transformation in Boron Under Shock Compression,” to be published in *Solid State Sciences*.

A. B. Zylstra, C. Yeamans, S. Le Pape, A. MacKinnon, M. Hohenberger, D. N. Fittinghoff, H. Herrmann, Y. Kim, P. B. Radha, P. W. McKenty, R. S. Craxton, and M. Hoppe, “Enhanced Direct-Drive Implosion Performance on NIF with Wavelength Separation,” to be published in *Physics of Plasmas*.

Conference Presentations

E. M. Campbell, “NIF: An Unexpected Journey and Lessons Learned to Secure ‘Projects of Scale,’” presented at the LLNL Seminar, virtual, 9 July 2020.

S.-W. Bahk, I. A. Begishev, R. G. Roides, D. H. Froula, J. Bromage, and J. D. Zuegel, “Application of Near-Field and Far-Field Beam Shaping Techniques for High-Power Lasers,” presented at Advanced Photonics Congress, virtual, 13–16 July 2020.

The following presentations were made at the BETHE Kickoff Workshop, virtual, 11–12 August 2020:

V. N. Goncharov, I. V. Igumenshchev, R. K. Follett, and T. J. B. Collins, “Advanced IFE Target Designs with Next-Generation Laser Technologies.”

P. Tzeferacos, A. B. Sefkow, C. Ren, R. Betti, J. R. Davies, and H. Wen, “A Simulation Resource Team for Innovative Fusion Concepts.”

K. L. Marshall, B. E. Ugur, and J. Travis, “Computational Modeling and Design of Liquid Crystal Materials for Applications in the Terahertz Regime” presented at SPIE Optics and Photonics, Liquid Crystals XXIV, virtual, 24–28 August 2020 (invited).

T. T. Simpson, D. Ramsey, P. Franke, N. Vafaei-Najafabadi, D. H. Froula, and J. P. Palastro, “The Self-Flying Focus: Nonlinear Spatiotemporal Control of Laser Intensity,” presented at ELI Summer School, virtual, 26–28 August 2020.

The following presentations were made at 9th EPS-QEOD Europhoton Conference, virtual, 30 August–4 September 2020:

G. W. Jenkins, C. Feng, and J. Bromage, “Overcoming Gas-Ionization Limits with Divided-Pulse Nonlinear Compression.”

B. Webb, S.-W. Bahk, I. A. Begishev, C. Dorrer, C. Feng, C. Jeon, M. Spilatro, R. Roides, J. D. Zuegel, and J. Bromage, “Full-Energy, Vacuum-Compatible, Single-Shot Pulse Characterization Method for Petawatt-Level Ultra-Broad Bandwidth Lasers Using Spatial Sampling.”

The following presentations were made at Laser Damage 2020, virtual, 13–16 September 2020:

E. M. Campbell, “A Vision of the Future for High-Power Lasers.”

V. Gruzdev and K. R. P. Kafka, “Multiphoton Absorption of Ultrashort Laser Pulses in Optical Materials of Multilayer Coatings at Near-Damage-Threshold Fluence.”

H. Huang, K. R. P. Kafka, and S. G. Demos, “Study of Electric-Field Enhancement Caused by Debris on Laser Optics.”

K. R. P. Kafka, B. N. Hoffman, A. A. Kozlov, and S. G. Demos, “Investigation of Excitation Dynamics in HfO₂ and SiO₂ Monolayers Using Subpicosecond Pump-and-Probe Damage Testing.”

M. S. Wei, “Omega Basic Science User Program Update,” Omega Laser Facility Users Group, virtual, 23–25 September 2020.

M. Zaghoo, H. Pantell, G. Tabak, L. Crandall, M. Huff, J. R. Rygg, G. W. Collins, S. X. Hu, V. V. Karasiev, D. N. Polsin, M. C. Marshall, R. Dias, E. Blackman, H. Aluie, P. M. Celliers, J. H. Eggert, D. E. Fratanduono, and S. Bonev, “Constraints from Mineral Physics on Thermal and Magnetic States of Exoplanets,” presented at Carnegie Earth and Planets Laboratory, virtual, 24 September 2020.

